

Mechanical behavior, tribological properties, and thermal stability of (AlCrNbSiTiVZr)N high entropy alloy nitride coatings and their application to Inconel 718 milling



W.H. Kao^{a,*}, Y.L. Su^b, J.H. Horng^{c,d}, Y.T. Cheng^b

^a Department of Automation Engineering & Institute of Mechatronoptic Systems Chienkuo Technology University, Changhua, Taiwan

^b Department of Mechanical Engineering, National Cheng Kung University, Tainan, Taiwan

^c Department of Power Mechanical Engineering, National Formosa University, Yunlin, Taiwan

^d Smart Machine and Intelligent Manufacturing Research Center, National Formosa University, Huwei, Yunlin, Taiwan

HIGHLIGHTS

- The annealed (AlCrNbSiTiVZr)N coatings showed improved mechanical, adhesive and tribological properties.
- The (AlCrNbSiTiVZr)N coatings showed excellent thermal stability.
- The high entropy alloy nitride-coated tools had a significantly improved cutting performance.

ARTICLE INFO

Keywords:

High entropy alloy
Thermal stability
Tribology
Machining performance

ABSTRACT

(AlCrNbSiTiVZr)N high entropy alloy nitride coatings were deposited on silicon wafers and WC substrates using a radio-frequency magnetron sputtering system with nitrogen flow rates of 0, 10, 15, and 20 sccm (coating codes: N0, N10, N15, and N20, respectively). The coatings were subsequently annealed in a vacuum at 950 °C for 1 h (coating codes: HN0, HN10, HN15, and HN20). The effects of the nitrogen flow rate on the composition, microstructure, mechanical properties, and tribological properties of the coatings were systematically examined. The N0 and N10 coatings had amorphous structures, whereas the N15 and N20 coatings had FCC structures. Among the as-deposited coatings, the N20 coating exhibited excellent mechanical properties and a superior tribological performance. All the annealed coatings showed an FCC structure and formed a V₂O₅ solid lubricant layer in ball-on-disk sliding tests. The lubricant layer reduced the coefficient of friction and led to a smooth friction curve. The annealed coatings additionally showed a high hardness, good adhesion strength, and excellent thermal stability. The mechanical and tribological properties of the HN20 coating were particularly impressive. In Inconel 718 milling trials, the N20-coated cutter showed an excellent machining performance, with significantly reduced flank wear, notch wear, and built-up edge adhesion.

1. Introduction

The development of advanced machining technologies and new super-hard alloys poses significant challenges to traditional manufacturing processes. The nickel-based alloys used in the aerospace industry, for example, have extremely high hardness and are thus not easily processed using traditional carbide-based tools. Consequently, improving the performance of cutting tools under arduous machining conditions, such as high speed and/or high temperatures, is a major

concern.

One of the most common methods for improving the wear and corrosion resistance of tool surfaces is depositing a protective coating using deposition processes such as cathode arc deposition (CAD), direct current magnetron sputtering (DCMS), radio frequency magnetron sputtering (RFMS), or unbalanced magnetron sputtering (UBMS). Among the coatings in common use nowadays, CrN coatings have a high corrosion resistance [1], while TiAlN coatings have a low coefficient of friction and high hardness [2]. In addition, diamond-like carbon (DLC)

* Corresponding author.

E-mail address: kaowh@ctu.edu.tw (W.H. Kao).

coatings have a low coefficient of friction and a high wear resistance [3]. Nitride-based coatings such as TiAlN and CrAlN increase the lifetime and performance of cutting and forming tools because of their high hardness, high elastic modulus, and superior mechanical properties [4]. However, even these coatings struggle to meet the harsh machining demands of the aerospace industry. Many of the nickel-based alloys used in this industry are classified as difficult-to-cut materials owing to their high work-hardening rates, high cutting temperatures, and tendency to form a built-up edge (BUE) on the cutting tool. Furthermore, the anti-oxidation temperatures of CrN, TiAlN, and DLC are 600 °C [5], 800 °C [6], and 350 °C [7], respectively. When these coatings exceed their respective anti-oxidation temperatures, they undergo structural changes, resulting in a significant reduction in their hardness. Consequently, their temperature resistance is lower than the cutting temperature generated during machining (typically around 950 °C). As a result, there is a need for new materials with a more robust mechanical, thermal, and tribological performance under extreme cutting conditions.

High-entropy alloys (HEAs) are a new class of materials that have attracted significant attention in recent decades. Composed of more than five elements, each accounting for 5–35 at.% of the total system composition, HEAs are characterized by four fundamental core effects: (1) high entropy, (2) sluggish diffusion, (3) lattice distortion, and (4) cocktail effect [8], which collectively imbue HEA coatings with high hardness [9], excellent wear resistance [10], and good thermal stability [6]. Various studies have shown that HEA systems consisting of five or six elements (e.g., (CrAlTiNbV)N [11], (AlCrNbSiTiV)N [12], and (AlCrMoTaTiZr)N [13]) have superior mechanical properties, good thermal stability, and a low wear rate. To improve the mechanical, tribological, and thermal properties of these alloy systems yet further, the present study proposes a new seven-element high entropy alloy nitride (HEAN) coating consisting of aluminum (Al), chromium (Cr), niobium (Nb), silicon (Si), titanium (Ti), vanadium (V), and zirconium (Zr). The proposed design thus draws on previous studies which showed that HEAN coatings composed of Al, Ti, and Zr exhibit a high hardness [14–16], while Cr and Nb enhance the thermal stability [17,18], and Si and V improve the wear resistance [19,20]. Furthermore, V forms a V₂O₅ solid lubricant at high temperatures, which reduces the friction coefficient during sliding [20], while zirconium nitride has high hardness, good wear resistance, and excellent thermal stability [21].

In the present study, (AlCrNbSiTiVZr)N coatings are deposited on silicon wafers and tungsten carbide (WC) substrates using a radio-frequency magnetron sputtering system with nitrogen flow rates of 0, 10, 15, and 20 sccm. The coatings are then annealed in a vacuum at 950 °C for 1 h. The effects of the nitrogen flow rate on the microstructure, mechanical properties, and tribological properties of the various coatings are systematically explored. Finally, the coating with the optimal tribological performance is deposited on WC four-flute corner-radius end-milling cutters for Inconel 718 milling trials.

2. Experimental details

2.1. Target and coating preparation

The (AlCrNbSiTiVZr)N coatings were deposited on silicon (100) wafers, WC disks ($\varnothing = 24$ mm, $h = 8$ mm), and WC cutting tools using a radio-frequency (RF) magnetron sputtering system (Teer-450C, Teer Coating, United Kingdom) with two AlCrNbSiTi targets, one Zr target, and one V target. The AlCrNbSiTi targets were prepared by hot pressing sintering and had chemical compositions of Al 34.1 at.%, Cr 22.0 at.%, Nb 11.0 at.%, Si 10.9 at.%, and Ti 22.0 at.%. The Zr and V targets were prepared via vacuum arc melting. The purities of the metal targets were all greater than 99.99 %. In addition, the dimensions were 300 mm × 109 mm × 10 mm. Before the coating process, the targets were pre-sputtered with Ar ions for 15 min at a flow rate of 20 sccm and a target current of 2 A to remove any surface contaminants. The base chamber pressure was set to 2.67×10^{-3} Pa, and the substrate was

rotated continuously at a speed of 2 rpm during the sputtering process. The deposition process commenced by coating a thin Zr interlayer on the substrate under an Ar flow rate of 20 sccm, substrate bias of –150 V for 6 min, and target current of 1.5 A. Due to the limitation of the target configuration, two high-entropy alloy targets, one V target, and one Zr target were required. Thus, no target position was available for installing a Cr target to sputter the interlayer. Consequently, Zr was selected as an interlayer material in its place. The adhesion test results showed that the Zr layer exhibited excellent adhesion, resulting in a high critical load of the coatings in the range of 80–90 N. Furthermore, after heat treatment, all the coatings showed a critical load in excess of 100 N, which represents a valuable contribution to sputter coating technology. The (AlCrNbSiTiVZr)N coatings were then deposited on the interlayer under an Ar flow rate of 20 sccm, AlCrNbSiTi target currents of 1.5 A, a V target current of 1.5 A, a Zr target current of 2 A, and a substrate bias of –35 V for 70 min. The coatings were deposited using nitrogen flow rates of 0, 10, 15, and 20 sccm, respectively. For convenience, the corresponding coatings were denoted as N0, N10, N15, and N20. The detailed deposition parameters are listed in Table 1.

Following the deposition process, the N0, N10, N15, and N20 coatings were annealed in vacuum at 950 °C for 1 h. The base pressure was set at 500 Pa. The samples were initially heated to 600 °C at a rate of 10 °C/min, maintained at this temperature for 20 min, and then heated further to 950 °C at a rate of 8 °C/min. They were then left in the furnace for 24 h to cool to room temperature. The corresponding coatings were denoted as HN0, HN10, HN15, and HN20, respectively.

2.2. Coating characterization

The compositions of the coatings were analyzed using an energy-dispersive spectrometer (EDS; ELITE, EDAX, USA). In addition, the crystallographic structures were characterized using an X-ray diffractometer (XRD; D8-Discover, Bruker, Germany) with Cu K α radiation. The analyses were conducted by symmetric XRD with a Bragg-Brentano setup using 20 scanning over a range of $2\theta = 20$ –80° at a scanning speed of 4°/min. The chemical characteristics of the coatings were determined using an X-ray photoelectron spectrometer (XPS; PHI 5000 VersaProbe, ULVAC. Inc., Japan) with Al-K α radiation. The microstructures were observed using a scanning electron microscope (SEM; SU5000, HITACHI, Japan). The surface roughness was measured by a white light interferometer (WLI; BRUKER/Contour GT-K, USA). The hardness and Young's modulus were measured using a nanoindentation tester (UNAT-M, ASMEC, Germany) under a maximum load of 10 mN. The maximum indentation depth was maintained at less than one-tenth of the coating thickness in all cases to avoid the substrate effect [16]. The adhesion strengths of the coatings were evaluated using a scratch tester (FM-POD-200NT, Freeform, Taiwan) fitted with a spherical diamond indenter tip with a diameter of 0.3 mm. The indenter was dragged across

Table 1
Experimental deposition parameters for (AlCrNbSiTiVZr)N coatings.

Various parameters		Fixed parameters	
Coating code	Nitrogen flow rate (sccm)	Interlayer parameters (Zr)	Main coating parameters (AlCrNbSiTiVZr)
N0	0	Deposited time: 6 min	Deposited time: 70 min
N10	10	Zr Target current: 1.5 A	AlCrNbSiTi target current: 1.5 A
N15	15	Argon flux: 20 sccm	V target current: 1.5 A
N20	20	Substrate bias: 150 V	Zr target current: 2 A
			Argon flux: 20 sccm
			Substrate bias: 35 V
			Base pressure: 2.67×10^{-3} Pa
			Working pressure: 0.33 Pa

the coating surface through a distance of 10 mm at a constant speed of 0.1 mm/s under a progressively increasing normal load of 0–100 N.

2.3. Tribological performance

The tribological properties of the coatings were evaluated using a ball-on-disk tribometer (KD-550U, Freeform, Taiwan) with an AISI 52100 steel ball with a diameter of 2.38 mm as the counterbody. The sliding tests were performed at a constant speed of 0.2 m/s with a normal load of 10 N, track diameter of 6 mm, and 9000 circular wear motions. The friction coefficient was continuously recorded throughout each test. The wear depth and wear rate of each sample were determined after the tests using the WLI. For each sample, the wear rate (K) was calculated as $K = (2\pi R \cdot A)/(L \cdot d)$, where R is the track radius, A is the cross-sectional wear area, L is the normal load, and d is the sliding distance. After the measurement process, the wear surfaces and elemental compositions of the coatings were observed using SEM and EDS, respectively.

2.4. Machining performance

Machining experiments were conducted on a 5-axis CNC machining center (DMU 70 eEvolution, Dechel-Macho, Germany) using Inconel 718 workpieces with dimensions of 140 mm × 140 mm × 60 mm. The workpieces contained 20.44 wt% Fe, 17.98 wt% Cr, and 51.78 wt% Ni, with small quantities of P, C, and Mn. The machining experiments were conducted using uncoated WC four-flute corner-radius end-milling cutters and cutters coated with the optimal (AlCrNbSiTiVZr)N coating. The milling process was performed under dry conditions using a climb milling technique with a cutting speed of 40 m/min, feed rate of 160 mm/min, depth of cut of 0.6 mm, cutting width of 1 mm, and rotational speed of 1280 rpm. The total cutting distance was 18 m. For each sample, the milling process was interrupted every 6 m of cutting distance to observe the morphology of the flank wear region using an optical microscope (OM; VHX-7000, KEYENCE, Japan). For convenience, the wear was measured only on two unconnected two-edge flutes, as shown in Fig. 1. For each flute, the flank wear depth was measured at three different positions, and the six measurements were averaged to obtain a representative value. The maximum notch wear length was similarly measured for both flutes and then averaged.

3. Results and discussion

3.1. Chemical composition

Fig. 2(a) and (b) show the elemental compositions of the as-

deposited and annealed (AlCrNbSiTiVZr)N coatings, respectively. (Note that the detailed elemental compositions (at.%) and relative EDS measurement error of each coating are listed in Table 2.) The relative error values of the EDS analysis results over three repeated measurements vary from 0.18 to 22.2 %. The minimum relative error, i.e., 53.0 ± 0.1 at.% (0.18 %), occurred for the N element in the N20 coating, while the maximum relative error, i.e., 3.6 ± 0.8 at.% (22.2 %), occurred for the C element in the HN15 coating.

Fig. 2(a) shows that in the absence of nitrogen, the contents of the seven metal elements in the AlCrNbSiTiVZr HEAN films vary between 5.6 at.% and 20.8 at.%. As the nitrogen flow rate increases, the nitrogen content increases rapidly at first and then tends toward a stable value as the flow rate increases to 15 and 20 sccm, respectively. In particular, the N contents of the NO, N10, N15, and N20 coatings are 0 at.%, 36.6 at.%, 52.3 at.%, and 53.0 at.%, respectively. This finding is consistent with those of previous studies [22,23], which reported that the nitrogen content of HEAN coatings saturates at approximately 50 at.%. All the coatings contain a small quantity of oxygen, which is thought to originate from either residual gas in the chamber during the deposition process or slight oxidation of the sample following its removal from the chamber. In previous studies by the current group [24,25], the oxygen content usually fell in the range of 3–9 at.%. Thus, the oxygen content of the NO coating in the present study (9.0 at.%) falls within a reasonable range. Generally, oxygen bonds or phases on the surfaces of metal or metal coatings are very common and unavoidable.

Fig. 2(b) shows that the N contents of the HN0, HN10, HN15, and HN20 coatings are 0 at.%, 24.4 at.%, 50.2 at.%, and 50.6 at.%, respectively. Thus, the N content is very similar to that of the as-deposited coatings. The O contents of the HN0 and HN10 coatings increase significantly from 9 to 2.7 at.% in the as-deposited condition to 42.0 at.% and 19.5 at.% in the annealed condition. However, the O contents of the HN15 and HN20 coatings are relatively unchanged after the annealing process (i.e., 2.3 and 2.4 at.% in the as-deposited condition and 3.2 and 2.5 at.% in the annealed condition). The annealing process was conducted under a relatively low degree of vacuum (500 Pa) with a setting temperature of up to 950 °C, and a time of 1 h. Under these conditions, the nitrogen-free annealed HN0 coating, which has poor oxidation resistance, can easily form chemical bonds with oxygen, and thus the surface of the coating forms an oxide layer. In contrast, for the high entropy alloy nitride (HEAN) coatings, N contents greater than 50 at.% lead to a high fraction of N-containing bonds. Nitrogen has high electronegativity and readily forms strong bonds with oxygen, thereby slowing the erosion of the coating by oxygen molecules [26]. Consequently, HEAN coatings with a high nitrogen content show good resistance in high-temperature oxidizing environments. The anti-oxidation resistance increases with increasing nitrogen content. Thus, in the

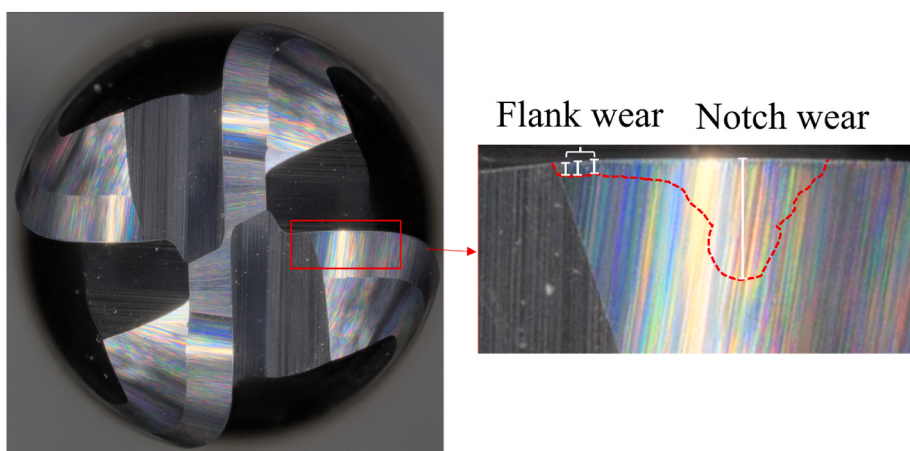


Fig. 1. Photograph of virgin tool with no wear. The red line shows schematically the typical wear region of the tool following milling. (For interpretation of the references to colour in this figure legend, the reader is referred to the Web version of this article.)

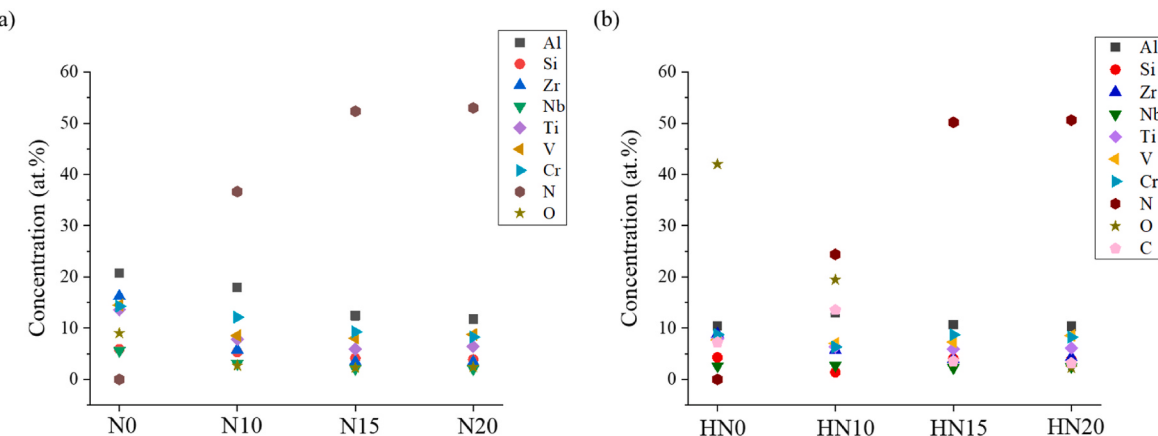


Fig. 2. EDS element contents in (a) as-deposited and (b) annealed $(\text{AlCrNbSiTiVZr})\text{N}$ coatings.

Table 2

Element compositions (at.%) of each coating determined by EDS.

Coating code	N	O	Al	Cr	Nb	Si	Ti	V	Zr	C
N0	0	9.0 ± 0.5	20.8 ± 0.3	14.3 ± 0.2	5.6 ± 0.1	5.9 ± 0.1	13.6 ± 0.2	14.5 ± 0.2	16.3 ± 0.3	0
N10	36.6 ± 1.1	2.7 ± 0.1	17.9 ± 0.2	12.1 ± 0.3	3.1 ± 0.1	5.3 ± 0.1	7.9 ± 0.4	8.6 ± 0.3	5.8 ± 0.1	0
N15	52.3 ± 0.3	2.3 ± 0.1	12.4 ± 0.1	9.3 ± 0.2	2.1 ± 0.1	4.1 ± 0.1	5.9 ± 0.1	8.0 ± 0.1	3.4 ± 0.1	0
N20	53.0 ± 0.1	2.4 ± 0.1	11.8 ± 0.1	8.3 ± 0.1	2.0 ± 0.1	3.9 ± 0.1	6.5 ± 0.1	8.8 ± 0.2	3.4 ± 0.1	0
HN0	0	42.0 ± 0.7	10.4 ± 0.3	8.8 ± 0.1	2.6 ± 0.2	4.3 ± 0.3	8.0 ± 0.2	7.7 ± 0.4	8.9 ± 0.2	7.3 ± 1.2
HN10	24.4 ± 1.0	19.5 ± 1.0	13.0 ± 0.1	6.3 ± 0.6	2.8 ± 0.1	1.4 ± 0.1	6.4 ± 0.5	7.0 ± 0.2	5.7 ± 0.1	13.6 ± 0.7
HN15	50.2 ± 0.7	3.2 ± 0.4	10.7 ± 0.1	8.7 ± 0.3	2.3 ± 0.1	4.1 ± 0.1	5.9 ± 0.5	7.3 ± 0.1	4.0 ± 0.2	3.6 ± 0.8
HN20	50.6 ± 0.5	2.3 ± 0.2	10.4 ± 0.2	8.3 ± 0.2	2.5 ± 0.1	3.9 ± 0.3	6.1 ± 0.7	8.6 ± 0.3	4.3 ± 0.2	3.2 ± 0.5

present HEAN coatings, the oxygen content reduces as the nitrogen flow rate increases.

All the annealed coatings contain carbon. According to Ref. [27], WC substrates undergo C diffusion at temperatures close to 1000 °C. In the present study, the annealing process was performed at 950 °C, and hence C diffused from the substrate to the coating. The EDS analysis results indicate that the HN0, HN10, HN15, and HN20 coatings have C contents of 7.3 at.%, 13.6 at.%, 3.6 at.%, and 3.2 at.%, respectively. It was shown in Ref. [28] that the stuffing effect of nitrogen results in the formation of a diffusion barrier. Consequently, for the present coatings, when the N content reaches the saturation level (approximately 52 at.%), the C diffusion effect is suppressed, and hence the coatings have a lower C content (<3.2 at.%). However, the C content of the HN0 coating is lower than that of the HN10 coating because the O content of HN0 (42.0 at.%) is higher than that of HN10 (19.5 at.%). In other words, the total at.% of all the elements in the coating system is equal to 100 %, and since the O content dominates in the HN0 coating, the C content is inevitably reduced.

3.2. Cross-sectional and surface morphologies

Fig. 3 presents cross-sectional SEM micrographs of the as-deposited and annealed $(\text{AlCrNbSiTiVZr})\text{N}$ coatings. (Note that the as-deposited coatings were prepared on Si substrates, while the annealed coatings were deposited on WC substrates since the coatings on the Si substrates were found to peel away from the substrate in the annealing process.) All the as-deposited coatings have a columnar structure. The N0 and N10 coatings have a dense structure, and hence the columnar features are less pronounced (Fig. 3(a) and (c)). However, the N15 and N20 coatings both have a distinct columnar structure, as shown in Fig. 3(e), owing to the enhanced adatom mobility of the coatings at high nitrogen flow rates, which allows the underlying crystals or grains to diffuse. Due to the anisotropic growth rate of the different crystal planes, some grains tend to overgrow and form columnar structures with faceted surfaces [23]. Following the annealing process, the HN0 and HN10 coatings have

dense and featureless structures, as shown in Fig. 3(b) and (d). This finding is reasonable because, as explained in a previous study [29], high temperatures tend to eliminate internal defects in coating structures and thus make the coatings denser. The HN15 and HN20 coatings both retain a columnar structure after annealing. However, the annealing process eliminates some gaps in the original columnar structure (Fig. 3(e) and (g)) and thus results in a denser structure, as shown in Fig. 3(f) and (h).

Table 3 shows the thicknesses of the various coatings. For the as-deposited coatings, the thickness reduces from 1.91 to 0.76 μm as the nitrogen flow rate increases from 0 to 20 sccm due to the target poisoning effect under high nitrogen concentrations in the sputtering chamber [30]. In particular, a high Ar flow rate increases the number of collisions between the Ar ions and the other ions in the deposition process, and therefore reduces the energy of the sputtered ions and the number of ions incident on the substrate [31]. However, in the present study, the introduction of nitrogen into the deposition process reduces the proportion of Ar in the sputtering chamber (since the Ar flow rate is fixed (20 sccm)). Consequently, the number of Ar ion collisions also reduces, and therefore the coating thickness should be increased. In fact, however, the coating thickness is significantly reduced. Thus, a higher nitrogen flow rate is inferred to result in target poisoning. The thickness of all the coatings increases after annealing due to the formation of an oxide layer on the coating surface at elevated temperatures. As shown in Fig. 2, the oxygen content of the HN0 and HN10 coatings is significantly higher than that of the N0 and N10 coatings, and thus the coating thickness increases more significantly. However, there is only a small change in the oxygen content of the HN15 and HN20 coatings (i.e., minimal oxidation occurs during annealing), and hence the coating thickness shows only a small increase compared to those of the as-deposited samples.

Fig. 4 presents SEM micrographs of the $(\text{AlCrNbSiTiVZr})\text{N}$ coatings. The mean cluster size of each coating is indicated in the corresponding micrograph, while the mean surface roughness values are shown in Table 3. The N0 and N10 coatings have cluster sizes of 57.5 and 59.7 nm,

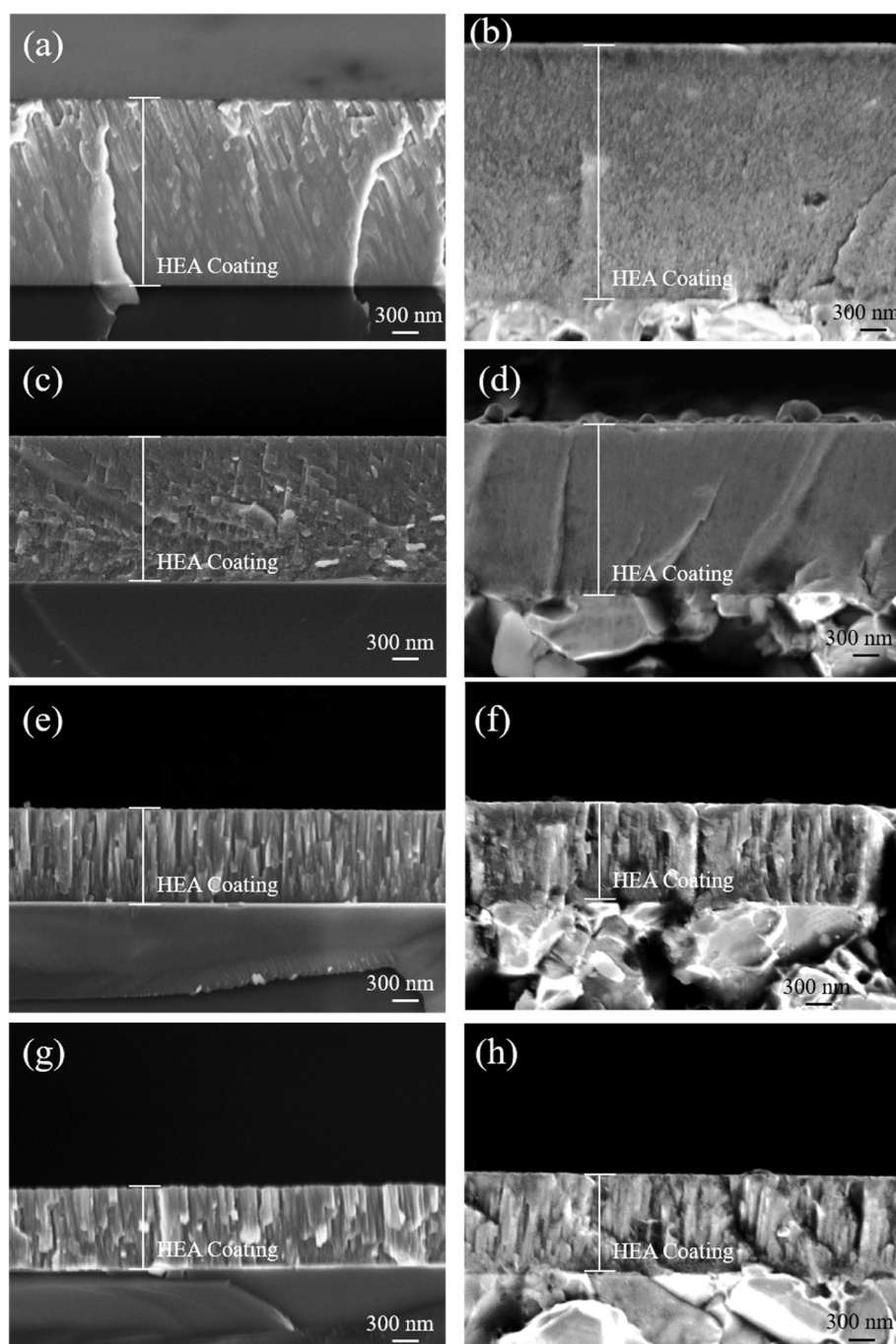


Fig. 3. Cross-sectional SEM micrographs of $(\text{AlCrNbSiTiVZr})\text{N}$ coatings: (a) N0, (b) HN0, (c) N10, (d) HN10, (e) N15, (f) HN15, (g) N20 and (h) HN20.

Table 3

Thickness, roughness, hardness, elastic modulus, hardness-to-elastic modulus (H/E) ratio, crystallite size, lattice parameter and adhesion strength of $(\text{AlCrNbSiTiVZr})\text{N}$ coatings.

Coating code	Thickness (μm)	Roughness Ra (nm)	Hardness (GPa)	Elastic modulus (GPa)	H/E	Crystallite size (nm)	Lattice parameter (\AA)	Adhesion strength Lc (N)
N0	1.91	20.0 ± 0.6	15.6 ± 2.3	324.8 ± 40.3	0.038	–	–	55.6 ± 4.3
N10	1.58	20.6 ± 0.4	21.6 ± 2.3	521.4 ± 89.3	0.041	–	–	81.7 ± 3.9
N15	1.02	23.9 ± 0.7	24.6 ± 3.8	564.5 ± 91.3	0.044	19.0	4.2333	89.9 ± 0.4
N20	0.76	24.3 ± 0.2	24.2 ± 3.2	484.7 ± 63.7	0.050	23.1	4.2382	98.4 ± 2.2
HN0	2.75	32.4 ± 0.1	20.7 ± 4.1	524.7 ± 103.2	0.039	57.5	4.3655	>100
HN10	1.78	28.8 ± 0.8	29.3 ± 3.6	684.4 ± 86.5	0.043	62.9	4.3655	>100
HN15	1.17	26.0 ± 0.4	31.6 ± 2.1	656.9 ± 65.7	0.048	64.3	4.3634	>100
HN20	0.85	26.0 ± 0.5	33.2 ± 3.5	612.0 ± 81.4	0.054	67.6	4.3657	>100

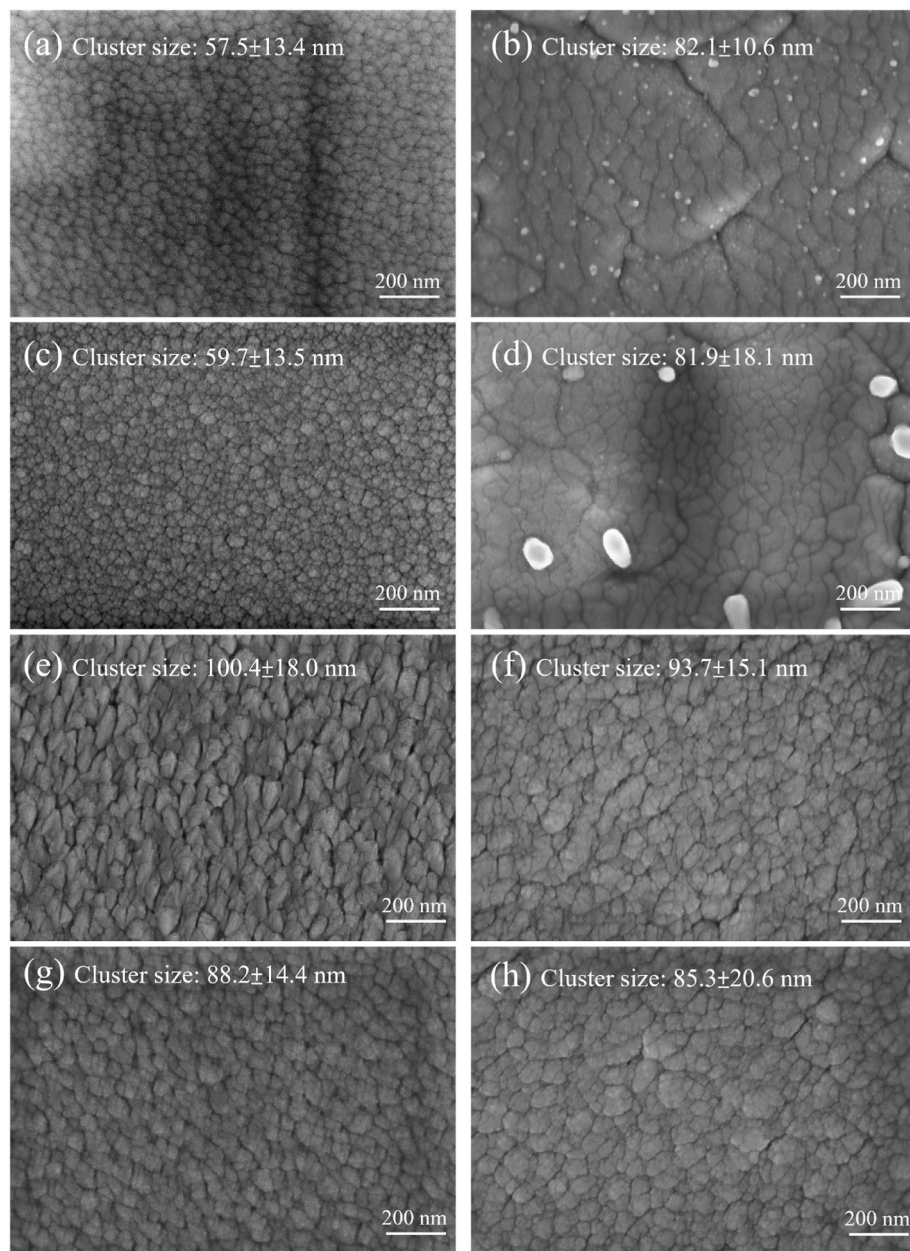


Fig. 4. Surface SEM micrographs of $(\text{AlCrNbSiTiVZr})\text{N}$ coatings: (a) N0, (b) HN0, (c) N10, (d) HN10, (e) N15, (f) HN15, (g) N20 and (h) HN20.

respectively. However, for the N15 and N20 coatings with a saturated nitrogen content, the cluster sizes increase to 100.4 nm and 88.2 nm, respectively. As shown in Fig. 4(a) and (c), the clusters on the surfaces of the N0 and N10 coatings have a dome-like appearance. Moreover, the two coatings have similar surface roughness values of $\text{Ra} = 20.0$ and 20.6 nm, respectively (Table 3). In contrast, the N15 coating has a loose faceted surface (Fig. 4(e)) and an increased surface roughness of $\text{Ra} = 23.9$ nm. The N20 coating consists mainly of loose dome-like clusters (Fig. 4(g)) and has a slightly higher surface roughness of $\text{Ra} = 24.3$ nm. The present findings are thus consistent with those of [23], which showed that a higher nitrogen flow rate increased the coating surface roughness.

Following the annealing process, the surfaces of the HN0 and HN10 coatings show a dense structure with increased cluster sizes of 82.1 nm and 81.9 nm, respectively, as shown in Fig. 4(b) and (d). However, the surface morphologies of the HN15 and HN20 coatings (Fig. 4(f) and (h)) are cauliflower-like and have cluster sizes of 93.7 nm and 85.3 nm, respectively, which are slightly smaller than those of the corresponding

as-deposited coatings. Among the four annealed coatings, the HN0 coating, with no nitrogen addition, shows the greatest increase in surface roughness following annealing (i.e., from $\text{Ra} = 20$ –32.4 nm). However, as the nitrogen content increases, the degree of increase in the surface roughness decreases. Thus, while the surface roughness of the HN10 coating increases from $\text{Ra} = 20.6$ –28.8 nm, that of the HN15 coating with a nitrogen content of 50.2 at.% only increases from $\text{Ra} = 23.9$ –26.0 nm, while that of the HN20 coating with 50.6 at.% nitrogen only increases from $\text{Ra} = 24.3$ –26.0 nm. In general, the EDS analysis results presented in Section 3.1 suggest that the greater roughness of the annealed coatings is associated with the formation of oxides. Taking the HN10 coating as an example, the oxygen content of the white particles shown in Fig. 4(d) is 27.7 at%, while the mean oxygen content of the coating is 19.5 at%. In other words, the white particles are assumed to be oxides, which increase the surface roughness. Notably, similar small white particles were also observed in a previous study by the present group [32], which found that the particles had a higher oxygen content than the mean oxygen content of the annealed coating and were thus

inferred to be oxides. However, for the coatings with a higher nitrogen content, e.g., the HN15 and HN20 coatings, the degree of oxidation is reduced, and hence the surface roughness increases only very slightly after annealing.

3.3. XRD analysis

Fig. 5(a) and (b) show the X-ray diffraction patterns of the as-deposited and annealed (AlCrNbSiTiVZr)N coatings, respectively. In **Fig. 5(a)**, the N0 and N10 coatings have a single broad peak, which indicates that they both have an amorphous structure because of the high mixing entropy effect of the seven-element HEA system and the large atomic size mismatch between the constituent elements. In contrast, the N15 and N20 coatings have simple face-center-cubic (FCC) structures because of the presence of TiN, VN, CrN, and NbN phases, all of which have FCC structures [33,34]. As described in Ref. [12], the FCC structure resulting from the combination of four FCC-forming binary nitrides can efficiently accommodate non-FCC binary nitrides. Accordingly, as the nitrogen flow rate increases, the structure tends to change from amorphous to FCC.

As shown in **Fig. 5(b)**, all the annealed coatings have an FCC structure, which suggests the occurrence of crystallization during the annealing process. However, after annealing, the peak intensity of the (200) plane of the coating became quite weak, while that of the (220) plane completely disappeared. According to previous studies [35,36], changes in the structure and defects after annealing affect the XRD peak intensity. Thus, it is possible that the structure still contains the (220) plane but its intensity is weaker than the XRD display resolution and is hence not visible in the XRD pattern. Furthermore, all the patterns show a distinctive (111) peak caused by the preferential growth of (111) oriented grains during annealing [34]. The HN15 and HN20 coatings retain their original FCC structures after annealing, and no new phases are formed. In other words, both films exhibit good thermal stability. In contrast, the HN0 and HN10 coatings transform from an amorphous structure to an FCC structure after heat treatment. However, as discussed later in Sections 3.4 and 3.5, the two coatings show an improved tribological performance compared to those in the as-deposited condition, and thus it is inferred that they too have good thermal stability.

According to Ref. [37], the better the crystallinity, the higher the intensity, and the narrower the full width at half maximum (FWHM). The N0 and N10 coatings exhibit amorphous states (**Fig. 5(a)**). However, after heat treatment, a crystalline phase is formed (**Fig. 5(b)**). Regarding the (111) crystalline phase, the N15 and N20 coatings both exhibit crystalline phases with intensities of 119 and 159, and FWHM values of 0.366 and 0.316 nm, respectively. The crystallinity of both coatings

improved after heat treatment, resulting in increased intensities of 605 (HN15) and 764 (HN20), and narrow FWHMs of 0.164 and 0.159 nm, respectively.

Table 3 lists the lattice parameters and crystallite sizes of the as-sputtered and annealed coatings. The N0 and N10 coatings both have amorphous structures and hence their grain sizes and lattice constants cannot be calculated. For the remaining coatings, the grain size and lattice constant can be determined from the (111) plane. In particular, the grain size can be calculated from the Scherrer Equation ($\tau = \frac{K\lambda}{\beta \cos \theta}$), while the lattice constant can be obtained from Bragg's law ($2d \sin \theta = n\lambda$), where the interplanar spacing (d) relation is given as ($d_{hkl} = a/\sqrt{(h^2 + k^2 + l^2)}$). The crystallite sizes of the N15 and N20 coatings before annealing were 19.0 and 23.1 nm, respectively. However, after annealing, the crystallite size increased, with the highest sizes being 64.3 and 67.6 nm for the HN15 and HN20 coatings, respectively. The lattice constant before annealing was about 4.23 Å, but increased to around 4.36 Å after annealing, with the highest value exhibited by the HN20 coating (4.3657 Å).

3.4. Mechanical properties

The hardness values and adhesion strengths of all the coatings are listed in **Table 3**. For the as-deposited coatings, the hardness increases from 15.6 GPa to 24.6 GPa as the nitrogen flow rate increases from 0 to 15 sccm. The higher hardness can be attributed to the formation of a greater number of hard nitrides and the incorporation of nitrogen atoms into the matrix, which enhances the solid-solution strengthening effect [38]. However, the hardness of the N20 coating, prepared using the maximum nitrogen flow rate, reduces very slightly to 24.2 GPa. According to Ref. [22], a nitride layer is formed on the surface of the alloy target as the nitrogen flow rate increases, which changes the reactive sputtering process in the chamber to direct nitride sputtering and decreases the coating hardness accordingly. Nonetheless, all the annealed coatings have a higher hardness than the as-deposited coatings owing to the increased crystallinity of the coating structure. In addition, the coatings become denser after annealing, as shown in **Fig. 3**. Moreover, annealing enhances the overall bonding strength between the target elements and the nitrogen because of the greater thermal energy provided at elevated temperatures [39]. Thus, even the HN0 and HN10 coatings, which have an amorphous structure in the as-deposited condition show much improved hardness values of 20.7 GPa and 29.3 GPa after the annealing process. Similarly, the hardness values of the HN15 and HN20 coatings increase to 31.6 GPa and 33.2 GPa, respectively.

The XPS results showed the presence of Al_2O_3 , Cr_2O_3 , ZrO_2 , Nb_2O_5 ,

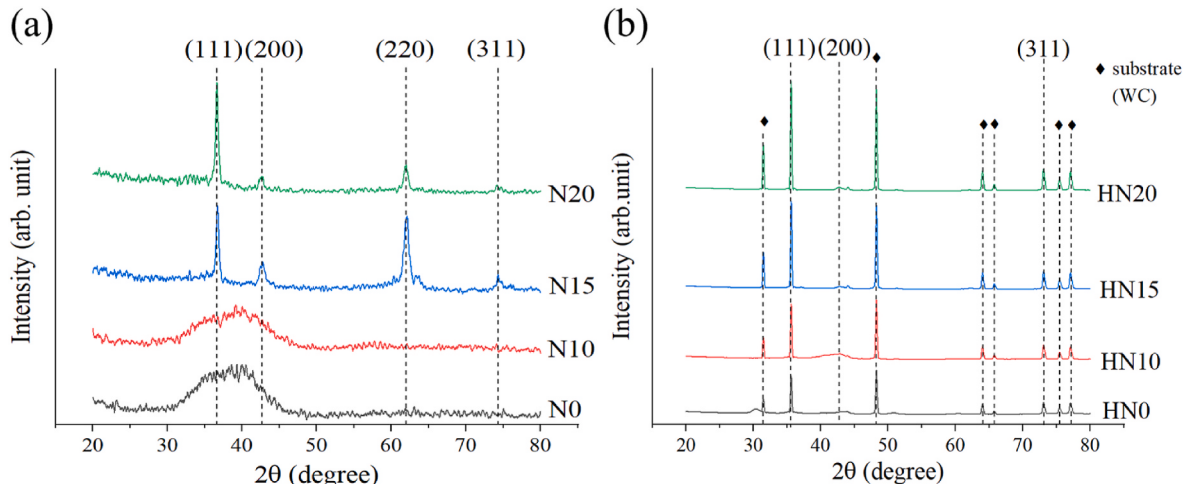


Fig. 5. XRD analysis results for (a) as-deposited and (b) annealed (AlCrNbSiTiVZr)N coatings.

TiO_2 , V_2O_3 , V_2O_5 , and SiO_2 oxides on the surfaces of the as-sputtered coatings. Subsequent heat treatment increased the oxide formation on the coating surfaces, among which the Al_2O_3 , ZrO_2 , and V_2O_3 oxides have a high hardness of 15–17 GPa, while the Cr_2O_3 , Nb_2O_5 , TiO_2 , V_2O_5 , and SiO_2 oxides have a low hardness of 2.4–10 GPa. Notably, the hardness values of all the oxides are lower than those of the heat-treated coatings. Thus, it can be inferred that they are not responsible for the higher coating hardness values observed after heat treatment.

Fig. 6 shows the XPS spectra of the N0 and N20 coatings. (Note that the spectra of these coatings are also representative of the bonding modes observed for the N10 and N15 coatings, respectively.) The N0 coating only forms Me–O and Me–Me bonds, i.e., Al–O, Cr–Cr, Cr–O, Nb–O, Zr–Zr, Zr–O, Ti–Ti, T–iO, V–V, V–O, and Si–Si. By contrast, the N20 coating forms not only Me–O and Me–Me bonds, but also Me–N bonds, i.e., Al–O, Cr–Cr, Nb–O, Zr–Zr, Ti–Ti, and V–V bonds, Al–N, Cr–N, Nb–N, Zr–N, Ti–N, V–N, and Si–N. Overall, when the nitrogen content

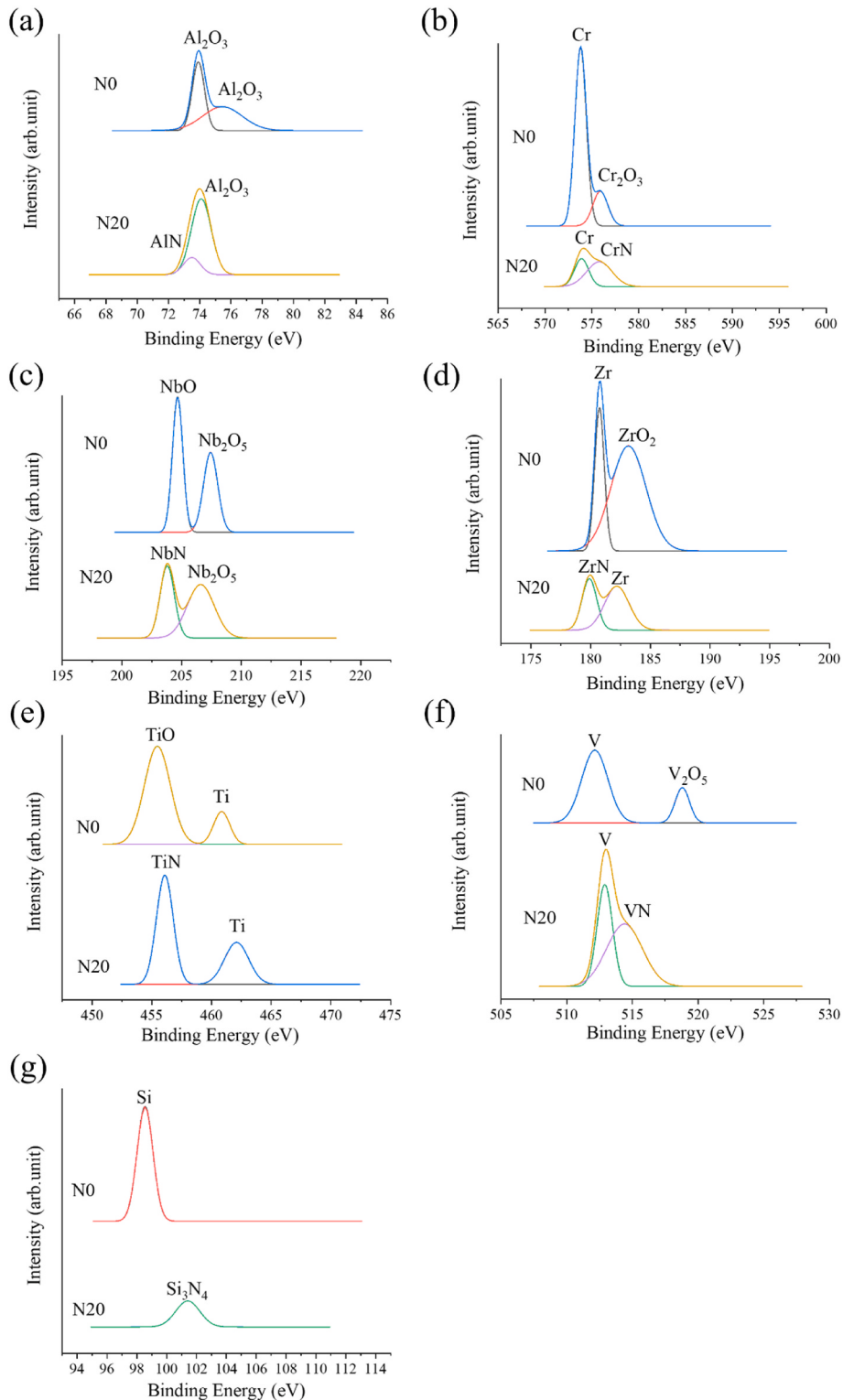


Fig. 6. XPS spectra of as-deposited N0 and N20 coatings: (a) Al 2p, (b) Cr 2p, (c) Nb 3d, (d) Zr 3d, (e) Ti 2p, (f) V 2p and (g) Si 2p.

reaches the saturation level in the N15 and N20 coatings, the coatings form Me–N bonds in addition to the original Me–Me and Me–O bonds, and only the Al and Nb elements retain Me–O bonds.

In general, the adhesion strength is a key factor in determining the performance and durability of protective thin-film coatings [40]. Fig. 7 shows the scratch track produced on the surface of the N10 coating during the scratch test. As shown, the coating began to peel continuously away from the substrate when the load reached 81.7 N. Thus, the critical load (L_c) of the coating was defined as 81.7 N. Table 3 lists the critical loads (i.e., adhesion strengths) of all the coatings. For the as-deposited coatings, the adhesion strength increases from 55.6 (N0) to 98.4 N (N20). The greater adhesion strength of the coatings with a higher nitrogen content can be attributed to the change in the coating structure from amorphous to FCC, in which the grain boundaries help resist plastic deformation [41]. The authors in Ref. [42] reported that coatings with a higher H/E ratio (i.e., hardness to elastic modulus ratio) can absorb more elastic energy before fracture failure. As shown in Table 3, the H/E ratio of the as-deposited coatings increases from 0.038 to 0.050 with an increasing nitrogen content, which also contributes to their higher adhesion strengths.

The annealed AlCrNbSiTiVZr)N coatings all have a critical load of more than 100 N. The high adhesion strength of these coatings can be attributed to their high H/E ratios, which imply that they can absorb all the elastic energy generated in the scratch test without failure. The superior critical loads of the annealed coatings can also be attributed in part to the greater number of crystalline phases with improved crystallinity, as shown in Fig. 5(b).

3.5. Tribological performance

3.5.1. Friction coefficient

Fig. 8(a) and (b) show the friction coefficient curves of the as-deposited and annealed (AlCrNbSiTiVZr)N coatings, respectively. The friction coefficient curves of the unannealed (WC) and annealed (HWC) substrates are also included for comparison purposes. The average friction coefficients of the coatings and substrates are listed in Table 4. As shown in Fig. 8(a), the WC substrate has a low and stable friction coefficient with a mean value of 0.17. Among the as-deposited samples, the native WC substrate has the lowest surface roughness ($R_a = 13.9$ nm), and the wear mechanism is dominated by abrasive wear, as discussed in Section 3.5.3. Consequently, the friction coefficient is reduced and the friction coefficient curve remains smooth over the entire duration of the sliding process. In contrast, the N0, N10, N15, and N20 coatings have high mean friction coefficients of 0.39, 0.40, 0.38, and 0.32, respectively. Among the four coatings, the N0 and N10 coatings contain V_2O_5 solid lubricant (as described below), but only the N10 coating shows a smooth friction coefficient curve. The oscillating friction curve of the N0 coating suggests the occurrence of adhesive wear during the sliding process. The N15 and N20 coatings, both without V_2O_5 solid lubricant, show a lower and more stable friction coefficient, which suggests that only minimal adhesion wear takes place during sliding. Nonetheless, the abrasive, oxidative, and adhesive wear of the wear pairs during the sliding process induces a large surface height

difference, which causes the friction coefficient to fluctuate as the sliding process proceeds.

As shown in Table 4, the average friction coefficient of the HWC substrate (0.39) is significantly higher than that of the original WC substrate (0.17). This can be attributed to the greater surface roughness of the HWC substrate ($R_a = 58.2$ nm) and the occurrence of oxidation and adhesive wear during sliding (see Section 3.5.3). The average friction coefficient of the HWC substrate is not only the highest of all the annealed wear pairs but also exhibits significant oscillations, as shown in Fig. 8(b). In contrast, the average friction coefficients of all the coatings reduce following the annealing process, as shown in Table 4. This is partly due to the formation of V_2O_5 solid lubricant on the annealed coating surfaces (see Fig. 9 for the illustrative case of the HN20 coating). The lower friction coefficient can also be partially attributed to the high H/E ratios of the annealed coatings (0.39–0.54) and their excellent adhesion strengths ($L_c > 100$ N).

As described above, the N0 and N10 coatings both contain V_2O_5 bonds. However, as the nitrogen content increases, the V_2O_5 bonds disappear, as shown in Fig. 6(f). For higher nitrogen contents, the coatings tend to form Me–N bonds rather than Me–O bonds (see Fig. 6). It was shown in Ref. [13] that, owing to the strong affinity of nitrogen atoms, it is easier for coating elements to form bonds with nitrogen when the nitrogen content increases. Thus, at higher nitrogen flow rates, the V_2O_5 content decreases, and under saturated nitrogen conditions (N15 and N20), no V_2O_5 is formed at all. Following the annealing process, all the coatings contain V_2O_5 , as described above. The V_2O_5 phase serves as a solid lubricant layer, which reduces the friction coefficients of all the coatings. For example, for the HN15 and HN20 coatings, which contain no V_2O_5 in the as-deposited condition, the friction coefficients drop significantly to 0.27 and 0.25, respectively. However, as for the as-deposited coatings, the number of V_2O_5 bonds reduces with an increasing nitrogen content. In particular, the V_2O_5 contents of the HN0, HN10, HN15, and HN20 coatings are 97.8 %, 30.7 %, 6.8 %, and 4.1 %, respectively (see Table 5).

3.5.2. Wear depth and wear rate

Table 4 shows the wear depths and wear rates of the substrates and coatings. The original WC substrate has a low wear depth and wear rate of $0.33 \mu\text{m}$ and $0.46 \times 10^{-6} \text{ mm}^3/\text{Nm}$, respectively. Among the as-deposited coatings, the N0 coating has the highest wear depth and wear rate of $2.71 \mu\text{m}$ and $8.64 \times 10^{-6} \text{ mm}^3/\text{Nm}$, respectively. The wear depth of the N0 coating is greater than the coating thickness ($1.91 \mu\text{m}$), which implies that the coating is completely worn through during the wear test. This finding is reasonable because the N0 coating has the lowest adhesion strength ($L_c = 55.6$ N) of all the coatings, and the friction coefficient curve fluctuates significantly, which suggests that the coating is severely damaged and generates a large amount of wear debris during sliding. The wear depth and wear rate of the N10 coating are reduced to $1.16 \mu\text{m}$ and $4.54 \times 10^{-6} \text{ mm}^3/\text{Nm}$, respectively, while those of the N15 coating are further reduced to $0.85 \mu\text{m}$ and $3.64 \times 10^{-6} \text{ mm}^3/\text{Nm}$. Finally, the wear depth and wear rate of the N20 coating are $0.13 \mu\text{m}$ and $0.36 \times 10^{-6} \text{ mm}^3/\text{Nm}$, respectively. In other words, as the nitrogen flow rate increases, the wear depth and wear rate decrease

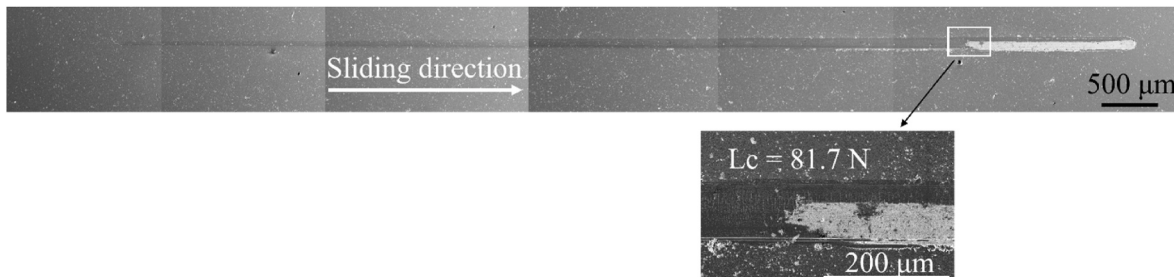


Fig. 7. SEM image of scratch track on surface of N10 coating.

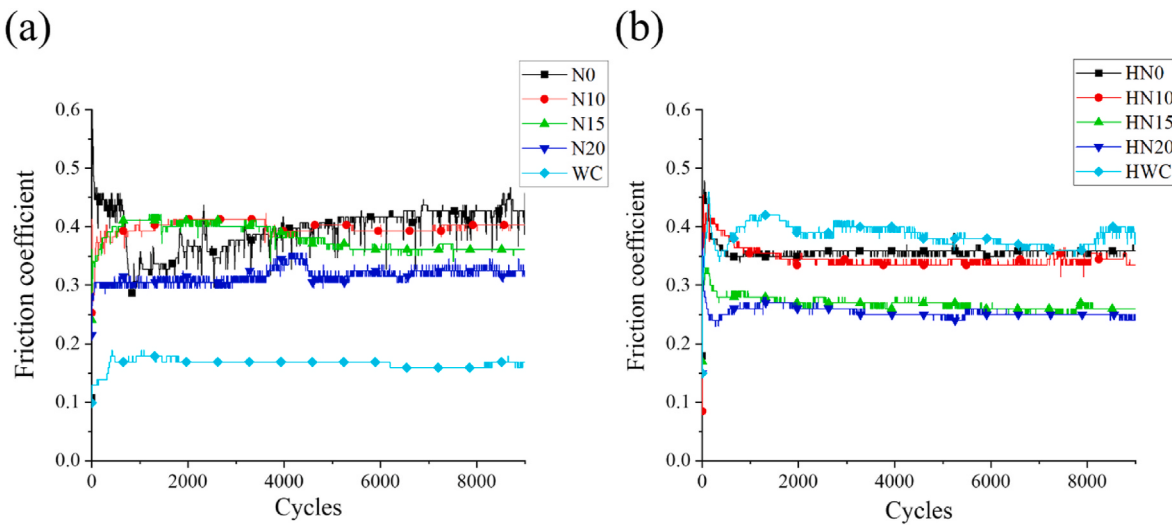


Fig. 8. Friction coefficient curves of: (a) as-deposited coatings and WC substrate and (b) annealed coatings and WC substrate.

Table 4

Friction coefficient, wear depth and wear rate of (AlCrNbSiTiVZr)N coatings and WC substrates sliding against AISI 52100 steel ball.

Coating code	Friction coefficient	Wear depth (μm)	Wear rate ($10^{-6} \text{ mm}^3/\text{Nm}$)
N0	0.40	2.71 ± 0.02	8.64 ± 1.35
N10	0.39	1.16 ± 0.06	4.54 ± 0.19
N15	0.38	0.85 ± 0.01	3.64 ± 0.32
N20	0.32	0.13 ± 0.03	0.36 ± 0.18
WC	0.17	0.33 ± 0.02	0.46 ± 0.02
HN0	0.36	0.38 ± 0.01	0.83 ± 0.06
HN10	0.34	0.31 ± 0.02	0.75 ± 0.13
HN15	0.27	0.26 ± 0.05	0.67 ± 0.31
HN20	0.25	0.10 ± 0.02	0.32 ± 0.14
HWC	0.39	0.36 ± 0.04	0.58 ± 0.05

Table 5

Content of V bonding in (AlCrNbSiTiVZr)N coatings based on XPS spectra of V 2p.

Coating code	V_2O_5 content (%)	V_2O_3 content (%)	V content (%)	VN content (%)
N0	21.0	0	79.0	0
N10	25.9	0	74.1	0
N15	0.0	0	80.8	19.2
N20	0.0	0	41.1	58.9
HN0	97.8	0	2.2	0
HN10	30.7	0	0	69.3
HN15	6.8	15.9	44.3	33.0
HN20	4.1	24.5	1.8	69.6

slightly from 0.33 to 0.36 μm, while the wear rate increases only from 0.46 to 0.58 $10^{-6} \text{ mm}^3/\text{Nm}$. Although the surface roughness of the HWC substrate increases after heat treatment and the substrate exhibits a higher coefficient of friction, its hardness hardly changes (from 15.8 GPa to 15.6 GPa). In other words, the HWC substrate has good thermal stability and thus exhibits good wear resistance. In a previous study by the present group [32], a Si₃N₄ ball with high hardness (14 GPa) was used as the counterbody in sliding tests against WC and HWC substrates. The wear rates of the substrates were almost identical. Thus, it was inferred that the HWC substrate had good thermal stability and wear resistance under the same heat treatment conditions. Among the various coatings, the HN0 coating shows the highest wear depth and wear rate of 0.38 μm and $0.83 \times 10^{-6} \text{ mm}^3/\text{Nm}$, respectively. However, these values are significantly lower than those of the corresponding as-deposited coating (2.71 μm and $8.64 \times 10^{-6} \text{ mm}^3/\text{Nm}$, respectively). Similarly, the wear depths of the HN10 and HN15 coatings reduce from 1.16 to 0.31 μm and 0.85 to 0.26 μm, respectively, while the wear rates decrease from 4.54 to $0.75 \times 10^{-6} \text{ mm}^3/\text{Nm}$ and 3.64 to $0.67 \times 10^{-6} \text{ mm}^3/\text{Nm}$, respectively. The wear depth and wear rate of the HN20 coating are just 0.10 μm and $0.32 \times 10^{-6} \text{ mm}^3/\text{Nm}$, respectively. In other words, the wear resistance of the annealed coatings also increases with an increasing nitrogen flow rate because of the improved adhesion strength ($L_c > 100 \text{ N}$), hardness, and H/E ratio.

In summary, the tribological properties of all the (AlCrNbSiTiVZr)N coatings are improved after annealing. Among the various coatings, the N20 and HN20 coatings show the best tribological properties before and after annealing, respectively. For example, compared with the substrate, the improvement effects of the N20 coating on the wear depth and wear rate are 60.6 % and 21.7 %, respectively, while those of the HN20 coating are 72.2 % and 44.8 %.

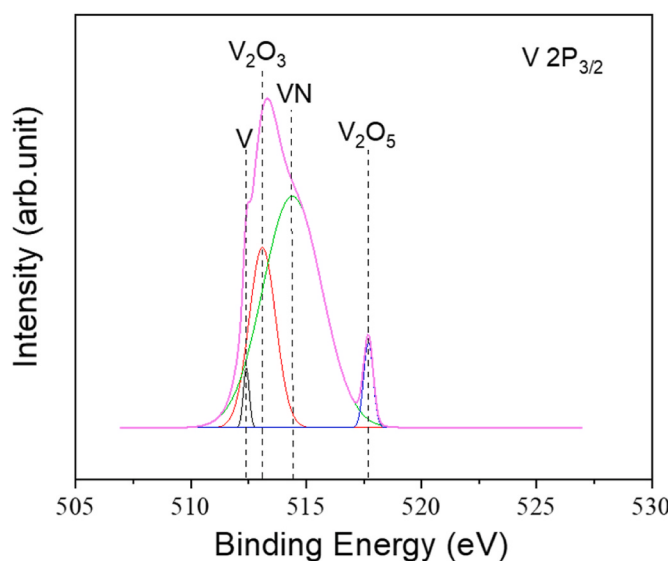


Fig. 9. V 2p spectra of HN20 coating obtained from XPS analysis.

continuously due to the corresponding increase in the adhesion strength, hardness, and H/E value (see Table 3). It should be noted that the present results are consistent with the findings of [40] that coatings with higher H/E ratios have an improved wear resistance.

Following annealing, the wear depth of the HWC substrate increases

3.5.3. Wear mechanisms

3.5.3.1. WC substrate wear mechanisms before and after annealing

Fig. 10(a) shows the wear track on the WC substrate. It is seen that the track contains many shallow grooves and locally oxidized areas. The O content in Region A (gray region) is 56.1 at.% and thus indicates the occurrence of severe oxidation. (Note that for convenience in the following discussions, an O content greater than 40 at.% is defined as severe oxidation, an O content less than 20 at.% is defined as mild oxidation and an O content between 20 at.% and 40 at.% is defined as moderate oxidation.) Region B (black block and ribbon regions) consists mainly of C (52.2 at.%), W (27.8 at.%), and O (16.1 at.%). The low oxygen content indicates that Region B suffers only mild oxidation wear. Thus, overall, the wear mechanism of the WC substrate is determined to be slight abrasion wear and severe oxidation wear.

Fig. 10(b) shows the wear track on the HWC substrate. The track contains many grooves and a large number of scattered oxidized spots (Region C, black spots) with an O content of 49.8 at.% (severe oxidation wear). In contrast, Region D has an O content of 26.6 at.%, which is indicative of moderate oxidation wear. Region C also has a Fe content of 16.6 at.%, where this Fe originates from the AISI 52100 steel ball during the wear process. In other words, Region C undergoes slight adhesive wear while sliding against the steel counterbody. The EDS results suggest that Fe adheres to the substrate during the wear process, which, together with the high surface roughness ($R_a = 58.2 \text{ nm}$), leads to the high and fluctuating friction coefficient curve observed in Section 3.5.1. Overall, the results indicate that the main wear mechanisms of the HWC substrate are severe oxidative wear, slight abrasive wear, and material adhesion. Nonetheless, these wear behaviors and mechanisms do not severely damage the HWC substrate (i.e., the wear depth ($0.36 \mu\text{m}$) is almost the same as that of the original WC substrate ($0.33 \mu\text{m}$) because

the annealing process does not significantly change the substrate hardness (i.e., WC hardness: 15.1 GPa; HWC hardness: 15.3 GPa).

3.5.3.2. $(AlCrNbSiTiVZr)N$ coating wear mechanisms before and after annealing

Since the wear mechanisms of the N10 and N15 coatings are similar, the wear mechanisms of the HN10 and HN15 are also similar. Thus, this section only considers the wear surfaces and wear mechanisms of the N0, HN0, N15, HN15, N20, and HN20 coatings.

Fig. 11(a) shows the wear track on the N0 coating. The track has a rough appearance. The EDS results show that Region A (gray rough area) has a high O content of 48.9 at.% and contains 16.1 at.% Fe. Region B (black ribbon regions) has an even higher O content of 55.5 at.% and a Fe content of 21.2 at.%. The wear track contains only very small quantities of the original coating elements, and hence it is inferred that the coating undergoes severe oxidation wear and adhesive wear during sliding. Collectively, these wear mechanisms, particularly the adhesive wear mechanism, result in the high and oscillating friction coefficient curves shown in **Fig. 8(a)**. In addition, the wear results presented in **Table 4** show that the wear depth of the N0 coating ($2.71 \mu\text{m}$) is greater than the coating thickness ($1.91 \mu\text{m}$). In other words, the wear scar penetrates the underlying substrate, and hence the C element of the WC substrate is detected in the wear track. Overall, the N0 coating has poor tribological properties because of its low adhesion strength ($L_c = 55.6 \text{ N}$), hardness (15.6 GPa), and H/E ratio (0.038).

Fig. 11(b) shows the wear track on the N15 coating. Region C (black smooth area) has a high N content of 51.2 at.%, and the contents of the other metal elements are all very close to those of the original coating. Furthermore, the O content is only 4.1 at.%. In other words, Region C undergoes virtually no wear during the sliding test. In contrast, Region D (white area) contains 26.8 at.% O, 25.9 at.% C, 24.3 at.% W, 5.8 at.% Fe, and very low quantities of the original coating elements. Thus, it is

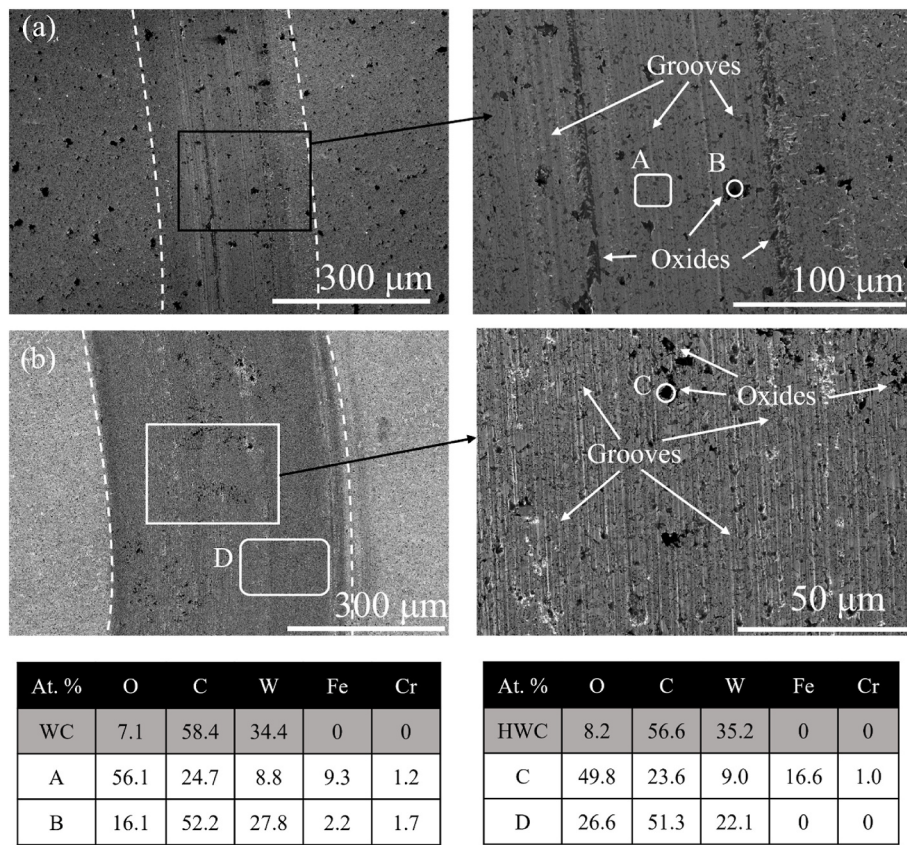
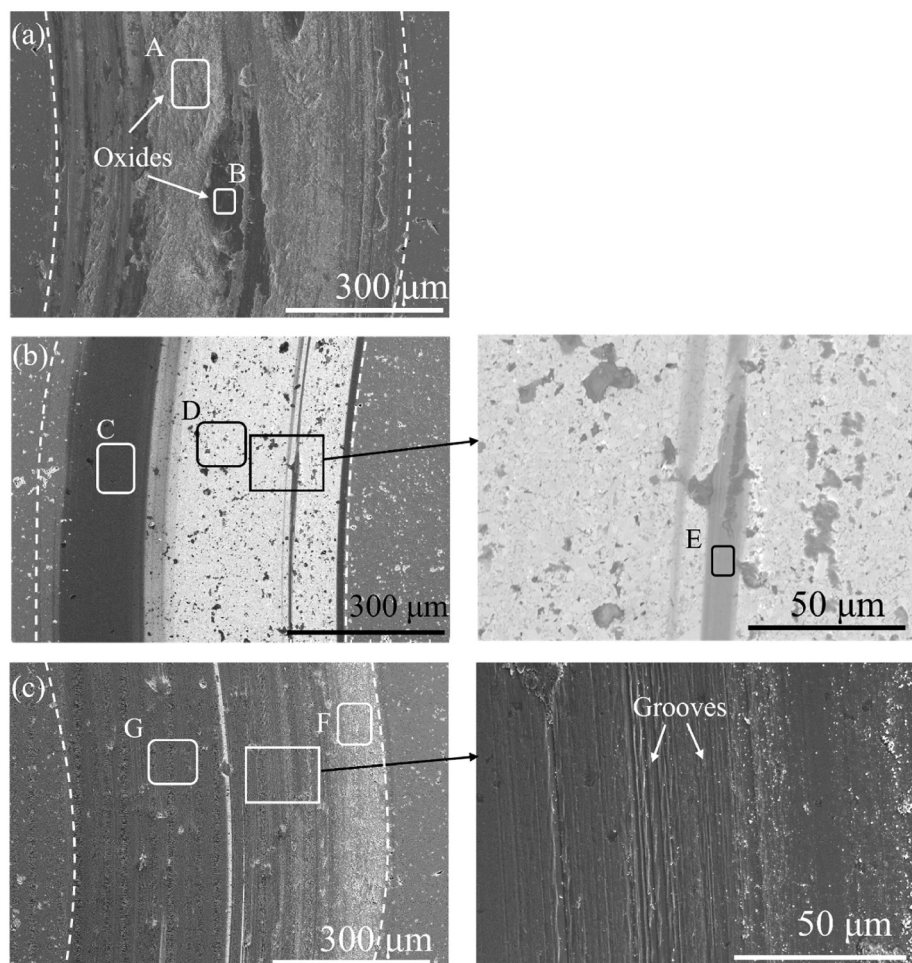


Fig. 10. SEM images and EDS analysis results for wear tracks on: (a) WC substrate and (b) HWC substrate.. (Note: for comparison purposes, the element compositions of the WC and HWC substrates are also shown.)



At. %	O	C	W	Fe	Al	Cr	Nb	Si	Ti	V	Zr	N
N0	9.0	0	0	0	20.8	14.3	5.6	5.9	13.6	14.5	16.3	0
A	48.9	13.8	1.3	16.1	4.3	3.3	1.2	1.6	2.9	3.2	3.4	0
B	55.5	11.1	0.3	21.2	2.6	2.1	0.8	0.8	1.7	1.8	2.1	0
N15	2.3	0	0	0	12.4	9.3	2.1	4.1	5.9	8.0	3.4	52.3
C	4.1	6.4	0.2	0.2	10.8	7.5	2.0	3.2	5.3	5.9	3.2	51.2
D	26.8	25.9	24.3	5.8	2.3	5.2	0.1	3.1	2.1	2.2	0.3	2.0
E	6.1	6.1	1.5	1.0	7.6	6.1	1.7	2.6	3.9	4.8	3.2	51.9
N20	2.4	0	0	0	11.8	8.3	2.0	3.88	6.5	8.8	3.4	53.0
F	21.9	12.9	0.1	4.4	5.6	4.1	1.4	1.6	3.6	4.6	2.4	37.6
G	13.4	6.9	0.1	2.2	6.9	5	1.8	1.9	4.2	5.4	2.9	49.3

Fig. 11. SEM images and EDS analysis results for wear tracks on: (a) N0, (b) N15, and (c) N20 coatings.. (Note: for comparison purposes, the original element compositions of the N0, N15 and N20 coatings are also shown.)

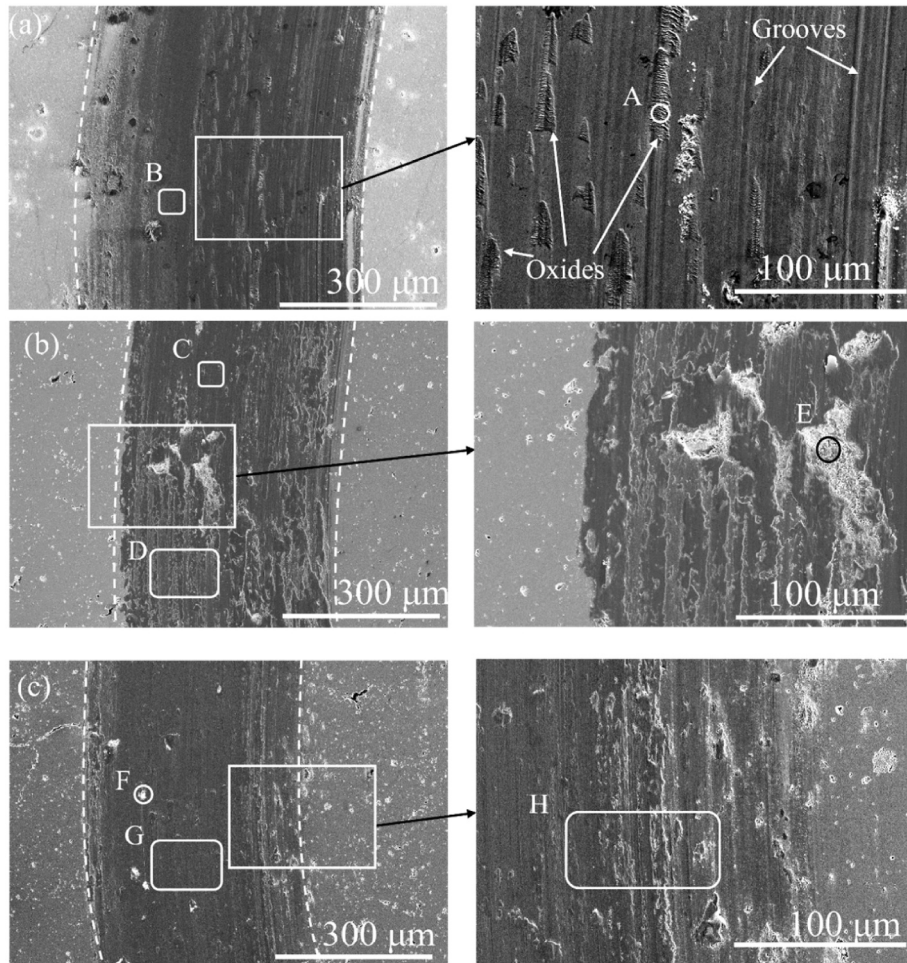
inferred that Region D experiences severe wear during the sliding process. For Region E (black banded area within the white area), the O content is just 6.1 at.%, while the nitrogen content is 51.9 at.%. Furthermore, the contents of the remaining coating elements are much lower than those of the original coating. Hence, although the white areas of the scratch track are heavily worn, some of the coating remains. Overall, the wear mechanism of the N15 coating is thus one of moderate oxidative wear accompanied by partial coating damage. Compared with

the N0 coating, the N15 coating still preserves some areas of residual coating. The improved tribological properties of the coating can be attributed to its higher adhesion strength (89.9 N), hardness (24.6 GPa), and H/E ratio (0.044).

Fig. 11(c) shows the wear track on the N20 coating. Although the track contains many mild grooves, it is smoother than the track on the N0 or N15 coating. The coating element contents of Regions F and G are similar to those of the original coating, while the O contents are 21.9 at.

% and 13.4 at.%, respectively. Overall, the results indicate that the N20 coating suffers only moderate localized oxidative wear. In other words, the coating has excellent wear resistance. The superior tribological properties of the coating are the result of its high hardness (24.2 GPa), high adhesion strength ($L_c = 98.4$ N), and high H/E ratio (0.05).

In general, the results presented in Fig. 11(a)–(c) show that the wear resistance of the as-deposited coatings increases with an increasing nitrogen content, which is consistent with the results presented in Section 3.5.2. As explained above, the improved wear resistance can be attributed to the greater adhesion strength, hardness, and H/E ratio of the



At. %	O	C	W	Fe	Al	Cr	Nb	Si	Ti	V	Zr	N
HN0	42.0	7.3	0	0	10.4	8.75	2.6	4.3	8.0	7.73	8.8	0
A	56.7	10.2	0.1	17.3	3.8	3.1	1.3	1.3	3.4	2.7	3.9	0
B	25.2	32.2	0.2	0.6	7.7	6.5	2.8	2.7	7.9	6.4	7.8	0
HN15	3.2	3.6	0	0	10.7	8.7	2.3	4.1	5.94	7.3	4.0	50.2
C	12.3	9.5	0.1	3.0	7.2	5.7	1.7	2.0	4.1	5.1	2.9	46.4
D	39.5	12.2	0.1	11.3	3.8	2.7	0.9	1.1	2.0	2.2	1.5	22.7
E	46.9	21.7	2.2	16.6	1.1	1.2	0.1	1.1	0.7	0.8	0.2	7.3
HN20	2.3	3.2	0	0	10.4	8.3	2.5	3.9	6.1	8.6	4.3	50.6
F	46.1	23.1	2.8	24.3	0.3	0.9	0.1	1.0	0.6	0.5	0	0.3
G	16.5	11.4	0.1	3.5	5.9	4.3	1.6	1.6	4.1	4.7	2.6	43.6
H	23.1	10.3	0.1	2.8	6.0	4.1	1.6	1.5	3.8	3.5	2.6	40.6

Fig. 12. SEM images and EDS analysis results for wear tracks on (a) HN0, (b) HN15 and (c) HN20 coatings.. (Note: for comparison purposes, the original element compositions of the HN0, HN15 and HN20 coatings are also shown.)

coatings with a higher nitrogen content. It is worth noting that although the N0 coating forms V_2O_5 solid lubricant (Table 5), the N15 and N20 coatings do not. Consequently, the finding that, among all the as-deposited coatings, the N20 coating has the best wear resistance indicates that the formation of V_2O_5 solid lubricant is not the main factor determining the wear resistance.

Fig. 12 shows the wear tracks on the surfaces of the HN0, HN15, and HN20 coatings. According to Ref. [27], WC substrates experience carbon diffusion at temperatures close to 1000 °C. The annealing process performed in the present study was conducted at 950 °C, and hence all the annealed coatings in Fig. 12 contain C. Fig. 12(a) shows the wear track on the HN0 coating. Compared with the N0 coating (Fig. 11(a)), the wear surface is smoother; however, it still contains some shallow grooves and scattered rough blocky areas (labeled as A in the SEM image). Region A is severely oxidized (O content 56.7 at.%) and shows evidence of material transfer from the steel counterbody (Fe content 17.3 at.%). Compared with Region A, Region B has a lower O content (25.2 at.%) and almost no Fe (0.6 at.%). Thus, the wear mechanism of the coating is inferred to be moderate oxidation wear, together with slight abrasion and adhesion wear. Consequently, the friction coefficient curve is more stable than that of the N0 coating, as shown in Fig. 8.

Fig. 12(b) shows the wear track on the HN15 coating. Region C (black smooth region) contains 46.4 at.% N and the contents of the other metal elements are fairly close to those of the original coating. However, the O content is approximately 12.3 at.%, which indicates the occurrence of slight oxidative wear. In contrast, Region D (rough surface) contains 39.5 at.% O and 11.3 at.% Fe. In other words, the rough region of the wear track suffers moderate oxidative wear but still retains some of the original coating material. The white flake areas in the wear track (Region E) have a high O content of 46.9 at.% and contain 16.6 at.% Fe. Moreover, the original coating elements exist in only very small quantities. Thus, it appears that the white flake areas experience severe oxidative wear and material (Fe) transfer from the counterbody during sliding. However, compared to the N15 coating (Fig. 11(b)), the HN15 coating remains largely intact during sliding, and thus significantly improves the wear resistance. The superior wear resistance can be attributed to the greater hardness (31.6 GPa), H/E ratio (0.48), and adhesion strength (>100 N) of the coating compared to the original coating.

Fig. 12(c) shows the wear track on the surface of the HN20 coating. The wear surface is quite smooth and contains only a small number of Fe oxides (Region F) with O and Fe contents of 46.1 and 24.3 at.%, respectively. Region G has a low O content of 16.5 at.%, which indicates mild oxidation wear. Region G also contains 43.6 at.% N and the remaining coating elements have quantities similar to those of the original coating. Hence, the black and smooth areas of the coating are almost undamaged. The rough areas on the edge of the wear track (Region H) have a higher O content of 23.1 at.%. However, the quantities of the other elements are very similar to those in Region G. Overall, the results indicate that the main wear mechanism of the HN20 coating is mild oxidation wear. The superior wear resistance of the HN20 coating stems from its highest adhesion (>100 N), hardness (33.2 GPa), and H/E ratio (0.054) among all the annealed coatings.

In summary, the wear resistance of all the coatings improves after annealing. Furthermore, the tribological properties of the annealed coatings improve with an increasing nitrogen content because of their greater adhesion strength, hardness, and H/E ratio. However, although the formation of V_2O_5 solid lubricant helps reduce the friction coefficient and improve its stability, it is not the main reason for the better wear resistance.

3.6. Machining performance

According to the experimental results presented in the previous sections, the N20 and HN20 coatings show the best mechanical properties and wear resistance among all the coatings. In industrial practice,

coated cutters are not heat-treated to reduce tool costs. Thus, to investigate the feasibility of the present coatings for real-world machining applications, the N20 coating was selected for milling tests performed on Inconel 718 workpieces.

Fig. 13 shows typical OM images of the flank wear and notch wear on the uncoated and N20-coated cutters after a total cutting distance of 18 m. The flank wear on the uncoated cutter is more significant than that on the coated cutter. In addition, the notch wear length of the N20-coated cutter (1071.6 μm) is smaller than that of the uncoated cutter (1194.8 μm).

Fig. 14(a) and (b) show the average flank wear and notch length, respectively, of the uncoated and N20 coated cutters after cutting distances of 6 m, 12 m, and 18 m. As shown in Fig. 14(a), the uncoated cutter has flank wears of 99.2 μm, 218.9 μm and 358.0 μm after cutting distances of 6, 12, and 18 m, respectively, while the N20 coated cutter shows flank wears of 80.0 μm, 109.2 μm, and 151.6 μm, respectively. In other words, compared to the uncoated cutter, the N20 coated cutter reduces the flank wear by 1.2, 2.0, and 2.4 times after cutting distances of 6 m, 12 m, and 18 m, respectively, corresponding to flank wear resistance improvements of 19.4 %, 50.1 %, and 57.7 %. As shown in Fig. 14(b), the uncoated cutter has notch wear lengths of 708.9 μm, 1135.6 μm, and 1194.8 μm after cutting distances of 6, 12, and 18 m, respectively. By contrast, those of the N20-coated cutter are 204.8 μm, 568.1 μm, and 1071.6 μm, respectively. Overall, the results presented in Fig. 14 confirm that the N20 coating effectively improves the wear resistance of the cutter and thus prolongs its service life.

Fig. 15 shows SEM images and the corresponding EDS element analysis and Ni element mapping results for the wear surfaces of the uncoated and N20-coated cutters, respectively. As shown in Fig. 15(a), the unworn surface of the uncoated tool contains 46.5 at.% C and 39.7 at.% W (Region A). Meanwhile, Region B in the wear area of the tool (white rectangle within white dotted lines) contains large amounts of Fe (17.9 at.%), Cr (18.0 at.%), and Ni (35.7 at.%). Region C has a wavy surface characteristic, which suggests the initial adhesion of workpiece material fragments during the milling process, followed by the subsequent peeling off and removal of these fragments by the shear action of the chip flow. Moreover, Region C contains 5.1 at.% Fe, 4.5 at.% Cr, and 5.2 at.% Ni. Fe, Cr, and Ni are the main components of Inconel 718, and thus their presence on the uncoated tool suggests the occurrence of BUE adhesion during the milling process. Fig. 15(b) shows the Ni element mapping results for the wear surface of the uncoated cutter. The mapping results show a high concentration of yellow spots in the area corresponding to Region B in Fig. 15(a), with a high Ni content of 35.7 at.% and a sparse concentration of yellow spots in the region corresponding to Region C in Fig. 15(a) with a low Ni concentration of 5.2 at.%. Thus, the results confirm that Region B experiences severe workpiece material adhesion (BUE), and the coating fractures in Region C.

Fig. 15(c) shows an SEM image of the wear surface of the N20-coated cutter, where Region A corresponds to the unworn region, and Regions B, C, and D correspond to the worn region. Region B has relatively high contents of Fe, Cr, and Ni (i.e., 14.1 at.%, 13.9 at.%, and 32.6 at.%, respectively), which indicates the occurrence of adhesion wear between the coating and the workpiece during the milling process. Region C has a higher content of C (45.2 at.%), W (11.6 at.%), and O (22.3 at.%), indicating local wear of the coating. In contrast, Region D (white rectangle within black dotted lines) has a lower Fe (10.4 at.%), Ni (15 at.%), and Cr (10.3 at.%) content than Region B, and a relatively lower C (22.0 at.%) and W (6.5 at.%) content than Region C, which implies that even though Region D is worn, some residual coating still remains on the wear surface. Fig. 15(d) shows the Ni element mapping results for the wear surface of the N20-coated cutter. Compared with the mapping results in Fig. 15(b), the number of small yellow spots is significantly reduced. In other words, the N20 coating effectively reduces the adhesion of the workpiece material.

The images presented in Fig. 15 show that compared to the uncoated N20 cutter, the coated cutter has a smoother wear surface with less

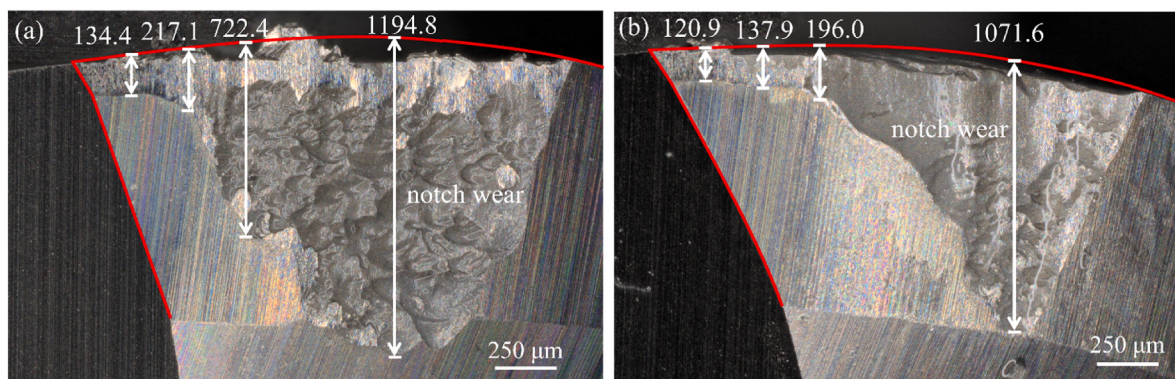


Fig. 13. OM images of flank wear (μm) and notch wear (μm) on: (a) uncoated cutter and (b) N20 coated cutter after cutting distance of 18 m.

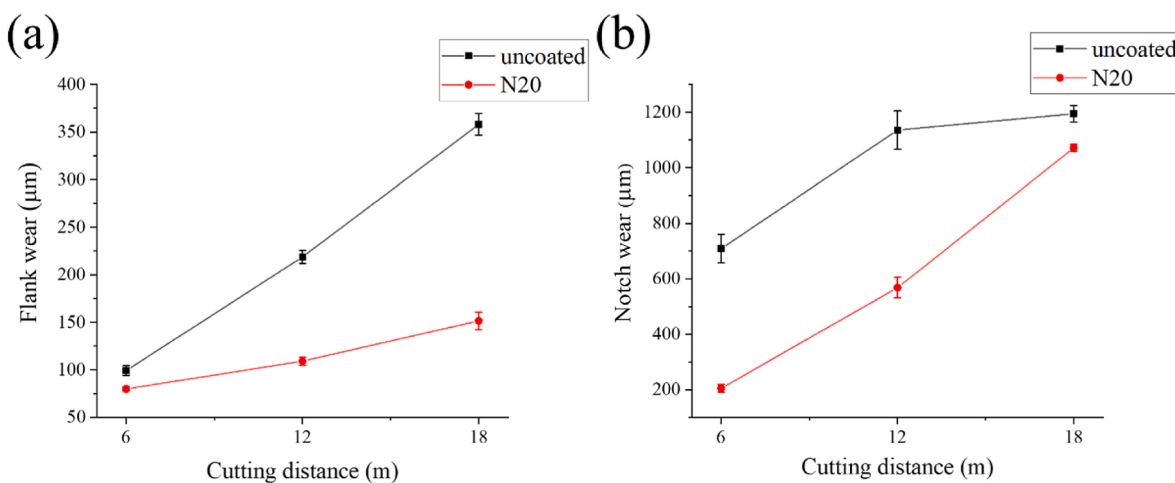


Fig. 14. (a) Average flank wear and (b) average notch wear of uncoated cutter and N20 coated cutter after cutting distances of 6 m, 12 m, and 18 m, respectively.

pronounced waves. This finding suggests that the N20 coating is beneficial for reducing the BUE adhesion effect, which in turn reduces the peeling of the coating from the cutter. In addition, the N20 coated cutter shows a significant reduction in the notch wear area. Therefore, the cutter has a longer tool life and a better machining performance.

4. Conclusions

(AlCrNbSiTiVZr)N coatings were deposited on WC substrates using an RF magnetron sputtering system with nitrogen flow rates ranging from 0 to 20 sccm. The coatings were then annealed for 1 h under a vacuum at 950 °C. The experimental results can be summarized as follows:

- (1) The nitrogen content of the N15 and N20 coatings remained almost unchanged after the annealing process since, when the nitrogen content of the coating saturates (at around 52 at.%), strong nitride bonds are formed, which imbue the coating with excellent thermal stability. The oxygen content of the annealed coatings was significantly higher than that of the as-deposited coatings with low nitrogen contents (N0 and N10). However, as the nitrogen content increased (N15 and N20), the oxygen content decreased significantly and was similar to that of the original as-deposited coatings.
- (2) The as-deposited nitrogen-free and low-nitrogen coatings (N0 and N10) had columnar cross-sectional structures. After annealing, both coatings exhibited dense and featureless structures. In contrast, the high-nitrogen-content coatings (N15 and N20) had a columnar structure both before and after annealing.

- (3) The hardness of the coatings generally increased with an increasing nitrogen content because of the solid-solution strengthening effect produced by the incorporation of N atoms into the matrix and the formation of Me-N bonds. Among the deposited coatings, the N15 and N20 coatings had similar hardness values of 24.6 and 24.2 GPa, respectively. However, after the annealing process, the hardness values increased to 31.6 and 33.2 GPa, respectively, due to the greater crystallinity of the coating structure and the enhanced bonding strength between the coating elements and nitrogen produced by the elevated annealing temperature.
- (4) Among all the coatings, the N20 and HN20 coatings showed the best wear resistance owing to their highest adhesion strength, hardness, and H/E ratio. Of the two coatings, the HN20 coating showed superior tribological properties due to the formation of V₂O₅ solid lubricant, which reduced the friction coefficient, and a higher hardness, H/E ratio, and adhesion strength. Compared to the uncoated HWC substrate, the HN20 coating improved the wear depth and wear rate by 72.2 % and 44.8 %, respectively.
- (5) The N20-coated tool showed a lower flank wear, shorter notch wear length, and less BUE adhesion than the uncoated tool. Thus, the N20 coating appears to be a promising protective coating material for nickel-based alloy machining applications.

CRediT authorship contribution statement

W.H. Kao: Data curation, Writing – review & editing, Data discussion, Writing – review & editing. **Y.L. Su:** Conceptualization, Methodology, Supervision, Data discussion. **J.H. Horng:** Investigation,

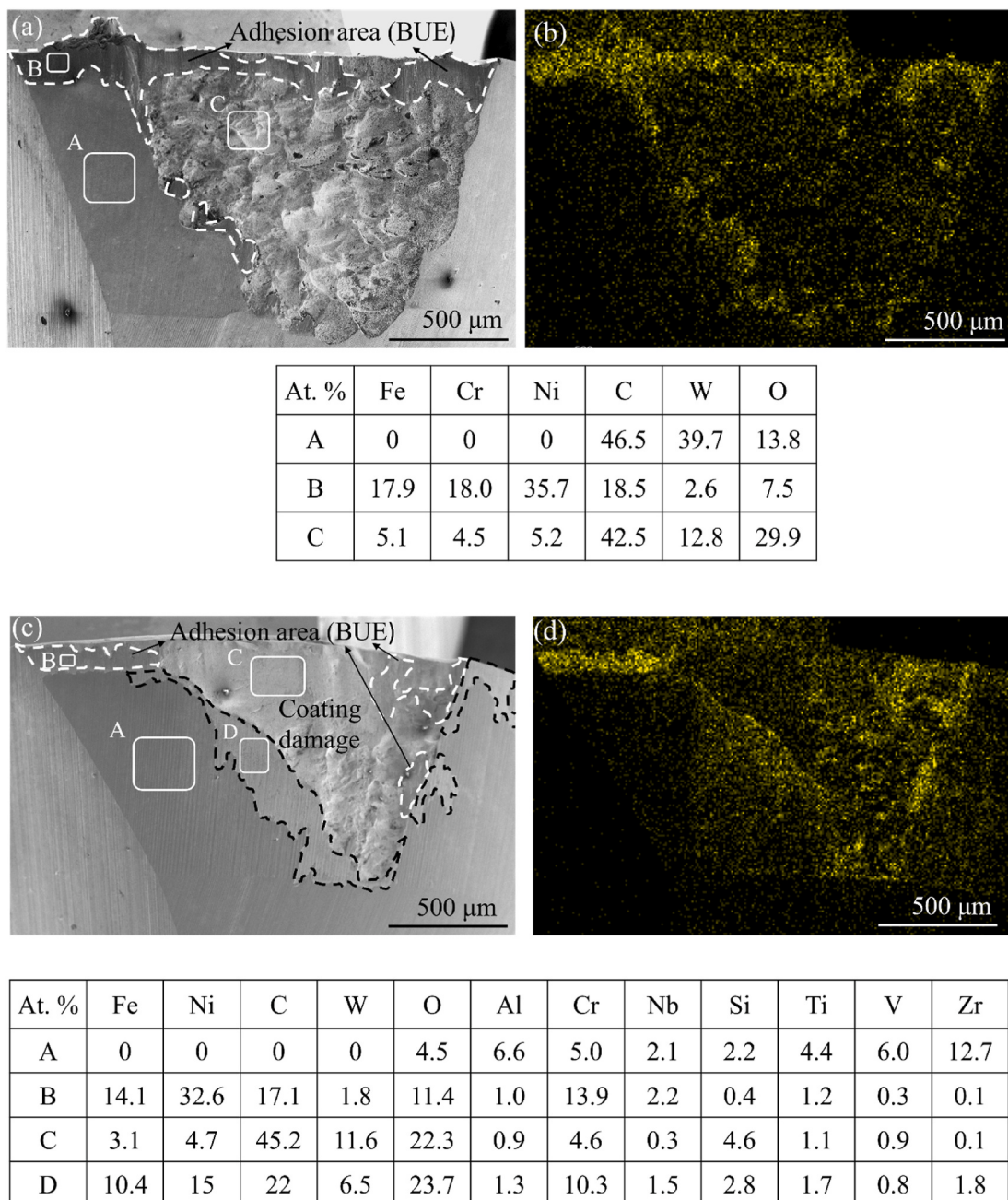


Fig. 15. SEM images and element mapping results after total cutting distance of 18 m: (a) wear surface of uncoated cutter, (b) Ni element mapping of uncoated cutter, (c) wear surface of N20 coated cutter, and (d) Ni element mapping of N20 coated cutter.

Verification, Data discussion. **Y.T. Cheng:** Sample preparation, Data detection, Data discussion, Writing – original draft.

Declaration of competing interest

The authors declare that they have no known competing financial interests or personal relationships that could have appeared to influence the work reported in this paper.

Data availability

No data was used for the research described in the article.

Acknowledgments

The authors gratefully acknowledge the financial support provided to this study by the Ministry of Science and Technology of Taiwan under Contract No. MOST 110-2221-E-270-002. The authors also appreciate the access given to EM000600, EM000700, ESCA000200, OTHER002200, and XRD001900 of MOST 100-2731-M-006-001 by the Core Facility Center of National Cheng Kung University.

References

- [1] B. Warcholinski, A. Gilewicz, Effect of substrate bias voltage on the properties of CrCN and CrN coatings deposited by cathodic arc evaporation, Vacuum 90 (2013) 145–150, <https://doi.org/10.1016/j.vacuum.2012.04.039>.
- [2] H.S. Cao, F.J. Liu, H. Li, W.Z. Luo, F.G. Qi, L.W. Lu, N. Zhao, X.P. Ouyang, Effect of bias voltage on microstructure, mechanical and tribological properties of TiAIN

- coatings, *Trans. Nonferrous Metals Soc. China* 32 (2022) 3596–3609, [https://doi.org/10.1016/S1003-6326\(22\)66042-4](https://doi.org/10.1016/S1003-6326(22)66042-4).
- [3] H. Fukui, J. Okida, N. Omori, H. Moriguchi, K. Tsuda, Cutting performance of DLC coated tools in dry machining aluminum alloys, *Surf. Coat. Technol.* 187 (2004) 70–76, <https://doi.org/10.1016/j.surcoat.2004.01.014>.
- [4] Y. Long, J. Zeng, D. Yu, S. Wu, Microstructure of TiAlN and CrAlN coatings and cutting performance of coated silicon nitride inserts in cast iron turning, *Ceram. Int.* 40 (7) (2014) 9889–9894, <https://doi.org/10.1016/j.ceramint.2014.02.083>. Part A).
- [5] H.C. Barshilia, N. Selvakumar, B. Deepthi, K.S. Rajam, A comparative study of reactive direct current magnetron sputtered CrAlN and CrN coatings, *Surf. Coat. Technol.* 201 (2006) 2193–2201, <https://doi.org/10.1016/j.surcoat.2006.03.037>.
- [6] W.J. Shen, M.H. Tsai, K.Y. Tsai, C.C. Juan, C.W. Tsai, J.W. Yeh, Y.S. Chang, Superior oxidation resistance of (Al_{0.34}Cr_{0.22}Nb_{0.11}Si_{0.11}Ti_{0.22})₅₀N₅₀ high-entropy nitride, *J. Electrochem. Soc.* 160 (2013) C531, <https://doi.org/10.1149/2.028311jcs>.
- [7] D.Y. Wang, C.L. Chang, W.-Y. Ho, Oxidation behavior of diamond-like carbon films, *Surf. Coat. Technol.* 120–121 (1999) 138–144, [https://doi.org/10.1016/S0257-8972\(99\)00350-3](https://doi.org/10.1016/S0257-8972(99)00350-3).
- [8] P.K. Huang, J.W. Yeh, Effects of substrate temperature and post-annealing on microstructure and properties of (AlCrNbSiTiVN) coatings, *Thin Solid Films* 518 (2009) 180–184, <https://doi.org/10.1016/j.tsf.2009.06.020>.
- [9] C.H. Lai, K.H. Cheng, S.J. Lin, J.W. Yeh, Mechanical and tribological properties of multi-element (AlCrTaTiZr)N coatings, *Surf. Coat. Technol.* 202 (2008) 3732–3738, <https://doi.org/10.1016/j.surcoat.2008.01.014>.
- [10] W.L. Lo, S.Y. Hsu, Y.C. Lin, S.Y. Tsai, Y.T. Lai, J.G. Duh, Improvement of high entropy alloy nitride coatings (AlCrNbSiTiMo)N on mechanical and high temperature tribological properties by tuning substrate bias, *Surf. Coat. Technol.* 401 (2020), 126247, <https://doi.org/10.1016/j.surcoat.2020.126247>.
- [11] X. Lu, C. Zhang, C. Wang, X. Cao, R. Ma, X. Sui, J. Hao, W. Liu, Investigation of (CrAlTiNbV)Nx high-entropy nitride coatings via tailoring nitrogen flow rate for anti-wear applications in aviation lubricant, *Appl. Surf. Sci.* 557 (2021), 149813, <https://doi.org/10.1016/j.apusc.2021.149813>.
- [12] P.K. Huang, J.W. Yeh, Effects of nitrogen content on structure and mechanical properties of multi-element (AlCrNbSiTiVN) coating, *Surf. Coat. Technol.* 203 (2009) 1891–1896, <https://doi.org/10.1016/j.surcoat.2009.01.016>.
- [13] K.H. Cheng, C.H. Lai, S.J. Lin, J.W. Yeh, Structural and mechanical properties of multi-element (AlCrMoTaTiZr)Nx coatings by reactive magnetron sputtering, *Thin Solid Films* 519 (2011) 3185–3190, <https://doi.org/10.1016/j.tsf.2010.11.034>.
- [14] W. Zhang, R. Tang, Z.B. Yang, C.H. Liu, H. Chang, J.J. Yang, J.L. Liao, Y.Y. Yang, N. Liu, Preparation, structure, and properties of an AlCrMoNbZr high-entropy alloy coating for accident-tolerant fuel cladding, *Surf. Coat. Technol.* 347 (2018) 13–19, <https://doi.org/10.1016/j.surcoat.2018.04.037>.
- [15] H. Cheng, W. Chen, X. Liu, Q. Tang, Y. Xie, P. Dai, Effect of Ti and C additions on the microstructure and mechanical properties of the FeCoCrNiMn high-entropy alloy, *Mater. Sci. Eng. A* 719 (2018) 192–198, <https://doi.org/10.1016/j.msea.2018.02.040>.
- [16] B. Ren, S.Q. Yan, R.F. Zhao, Z.X. Liu, Structure and properties of (AlCrMoNiTi)Nx and (AlCrMoZrTi)Nx films by reactive RF sputtering, *Surf. Coat. Technol.* 235 (2013) 764–772, <https://doi.org/10.1016/j.surcoat.2013.08.064>.
- [17] C. Huang, Y. Zhang, J. Shen, R. Vilar, Thermal stability and oxidation resistance of laser clad TiVCrAlSi high entropy alloy coatings on Ti-6Al-4V alloy, *Surf. Coat. Technol.* 206 (2011) 1389–1395, <https://doi.org/10.1016/j.surcoat.2011.08.063>.
- [18] M. Braic, V. Braic, M. Balaceanu, C.N. Zaita, A. Vladescu, E. Grigore, Characteristics of (TiAlCrNbY)C films deposited by reactive magnetron sputtering, *Surf. Coat. Technol.* 204 (2010) 2010–2014, <https://doi.org/10.1016/j.surcoat.2009.10.049>.
- [19] K. Oguri, T. Arai, Tribological properties and characterization of diamond-like carbon coatings with silicon prepared by plasma-assisted chemical vapour deposition, *Surf. Coat. Technol.* 47 (1991) 710–721, [https://doi.org/10.1016/0257-8972\(91\)90344-V](https://doi.org/10.1016/0257-8972(91)90344-V).
- [20] A.A. Voedovin, C. Muratore, S.M. Aouadi, Hard coatings with high temperature adaptive lubrication and contact thermal management: review, *Surf. Coat. Technol.* 257 (2014) 247–265, <https://doi.org/10.1016/j.surcoat.2014.04.046>.
- [21] H.M. Tung, J.H. Huang, D.G. Tsai, C.F. Ai, G.P. Yu, Hardness and residual stress in nanocrystalline ZrN films: effect of bias voltage and heat treatment, *Mater. Sci. Eng.* 500 (2009) 104–108, <https://doi.org/10.1016/j.msea.2008.09.006>.
- [22] P. Cui, W. Li, P. Liu, K. Zhang, F. Ma, X. Chen, R. Feng, P.K. Liaw, Effects of nitrogen content on microstructures and mechanical properties of (AlCrTiZrHf)N high-entropy alloy nitride films, *J. Alloys Compd.* 834 (2020), 155063, <https://doi.org/10.1016/j.jallcom.2020.155063>.
- [23] S.C. Liang, D.C. Tsai, Z.C. Chang, H.S. Sung, Y.C. Lin, Y.J. Yeh, M.J. Deng, F. S. Shieh, Structural and mechanical properties of multi-element (TiVCrZrHf)N coatings by reactive magnetron sputtering, *Appl. Surf. Sci.* 258 (2011) 399–403, <https://doi.org/10.1016/j.apsusc.2011.09.006>.
- [24] W.H. Kao, Y.L. Su, J.H. Horng, W.C. Wu, Mechanical, tribological, anti-corrosion and anti-glass sticking properties of high-entropy TaNbSiZrCr carbide coatings prepared using radio-frequency magnetron sputtering, *Mater. Chem. Phys.* 268 (2021), 124741, <https://doi.org/10.1016/j.matchemphys.2021.124741>.
- [25] W.H. Kao, Y.L. Su, J.H. Horng, C.M. Wu, Structure, mechanical properties and thermal stability of nitrogen-doped TaNbSiZrCr high entropy alloy coatings and their application to glass moulding and micro-drills, *Surf. Coat. Technol.* 405 (2021), 126539, <https://doi.org/10.1016/j.surcoat.2020.126539>.
- [26] A. Farhadizadeh, J. Vlček, J. Houška, S. Havíř, R. Čerstvý, M. Červená, M. Matas, Effect of nitrogen content on high-temperature stability of hard and optically transparent amorphous Hf-Y-Si-B-C-N coatings, *Ceram. Int.* 46 (2023) 6086–6093, <https://doi.org/10.1016/j.ceramint.2022.10.250>.
- [27] S. Odérols, B. Kaplan, M. Kritikos, M. Johansson, S. Norgren, Experimental and theoretical study of the microscopic crater wear mechanism in titanium machining, *Wear* 376–377 (2017) 115–124, <https://doi.org/10.1016/j.wear.2017.01.104>.
- [28] M. Damayanti, T. Sritharan, S.G. Mhaisalkar, Z.H. Gan, Effects of dissolved nitrogen in improving barrier properties of ruthenium, *Appl. Phys. Lett.* 88 (2006), 044101, <https://doi.org/10.1016/j.apl.2012.1.2167610>.
- [29] Y.C. Lin, S.Y. Hsu, R.W. Song, W.L. Lo, Y.T. Lai, S.Y. Tsai, J.G. Duh, Improving the hardness of high entropy nitride (Cr_{0.35}Al_{0.25}Nb_{0.12}Si_{0.08}V_{0.20})N coatings via tuning substrate temperature and bias for anti-wear applications, *Surf. Coat. Technol.* 403 (2020), 126417, <https://doi.org/10.1016/j.surcoat.2020.126417>.
- [30] L. Chen, W. Li, P. Liu, K. Zhang, F. Ma, X. Chen, H. Zhou, X. Liu, Microstructure and mechanical properties of (AlCrTiZrV)Nx high-entropy alloy nitride films by reactive magnetron sputtering, *Vacuum* 181 (2020), 109706, <https://doi.org/10.1016/j.vacuum.2020.109706>.
- [31] V. Jain, M.C. Biesinger, M.R. Linford, The Gaussian-lorentzian sum, product, and convolution (voigt) functions in the context of peak fitting X-ray photoelectron spectroscopy (XPS) narrow scans appl, *Surf. Sci.* 447 (2018) 548–553, <https://doi.org/10.1016/j.apsusc.2018.03.190>.
- [32] W.H. Kao, Y.L. Su, Y.J. Lin, Mechanical, tribological, and anti-corrosion properties of nitrogen-doped AlCrNbSiTiMoW high-entropy coatings, *J. Mater. Eng. Perform.* *J. Mater. Eng. Perform.* (2023), <https://doi.org/10.1007/s11665-023-08394-3> published on line: 9 June.
- [33] D.C. Tsai, Y.L. Huang, S.R. Lin, D.R. Jung, S.Y. Chang, F.S. Shieh, Structure and mechanical properties of (TiVCr)N coatings prepared by energetic bombardment sputtering with different nitrogen flow ratios, *J. Alloys Compd.* 509 (2011) 3141–3147, <https://doi.org/10.1016/j.jallcom.2010.12.026>.
- [34] M.H. Hsieh, M.H. Tsai, W.J. Shen, J.W. Yeh, Structure and properties of two Al–Cr–Nb–Si–Ti high-entropy nitride coatings, *Surf. Coat. Technol.* 221 (2013) 118–123, <https://doi.org/10.1016/j.surcoat.2013.01.036>.
- [35] P. Moazzeni, M.R. Toroghinejad, Enhancement of mechanical properties of a novel single phase Ni_{1.5}FeCrCu_{0.5} HEA through cold rolling and subsequent annealing, *Mater. Sci. Eng.* 848 (2022), 143360, <https://doi.org/10.1016/j.msea.2022.143360>.
- [36] Q. Wang, H. Wang, T. Gao, L. Qian, L. Zeng, Q. Chen e, X. Liu, Microstructure evolution and mechanical properties of an annealed dual-phase CrFeCoNiAl_{0.7} high-entropy alloy, *Intermetallics* 149 (2022), 107657, <https://doi.org/10.1016/j.intermet.2022.107657>.
- [37] D.L. Ma, Q.Y. Deng, H.Y. Liu, Y.T. Li, Y.X. Leng, Microstructure and properties of Ti₂AlN thin film synthesized by vacuum annealing of high power pulsed magnetron sputtering deposited Ti/AlN multilayers, *Surf. Coat. Technol.* 425 (2021), 127749, <https://doi.org/10.1016/j.surcoat.2021.127749>.
- [38] Y. Zhao, S. Chen, Y. Chen, S. Wu, W. Xie, W. Yan, S. Wang, B. Liao, S. Zhang, Super-hard and anti-corrosion (AlCrMoSiTi)Nx high entropy nitride coatings by multi-arc cathodic vacuum magnetic filtration deposition, *Vacuum* 195 (2022), 110685, <https://doi.org/10.1016/j.vacuum.2021.110685>.
- [39] H.W. Chang, P.K. Huang, J.W. Yeh, A. Davison, C.H. Tsau, C.C. Yang, Influence of substrate bias, deposition temperature and post-deposition annealing on the structure and properties of multi-principal-component (AlCrMoSiTi)N coatings, *Surf. Coat. Technol.* 202 (2008) 3360–3366, <https://doi.org/10.1016/j.surcoat.2007.12.014>.
- [40] M. Othman, A.R. Bushroa, A. R, Evaluation techniques and improvements of adhesion strength for TiN coating in tool applications: a review, *J. Adhes. Sci. Technol.* 29 (2015) 569–591, <https://doi.org/10.1080/01694243.2014.997379>.
- [41] W.Z. Abuzaid, M.D. Sangid, J.D. Carroll, H. Sehitoglu, J. Lambros, Slip transfer and plastic strain accumulation across grain boundaries in Hastelloy X, *J. Mech. Phys. Solid.* 60 (2012) 1201–1220, <https://doi.org/10.1016/j.jmps.2012.02.001>.
- [42] A. Leyland, A. Matthews, On the significance of the H/E ratio in wear control: a nanocomposite coating approach to optimised tribological behaviour, *Wear* 246 (2000) 1–11, [https://doi.org/10.1016/S0043-1648\(00\)00488-9](https://doi.org/10.1016/S0043-1648(00)00488-9).